Article

Optical manipulation of the charge-density-wave state in RbV_3Sb_5

https://doi.org/10.1038/s41586-024-07519-5

Received: 31 July 2023

Accepted: 3 May 2024

Published online: 12 June 2024

Check for updates

Yuqing Xing[1,6], Seokjin Bae[1,6], Ethan Ritz[2], Fan Yang[2], Turan Birol[2], Andrea N. Capa Salinas[3], Brenden R. Ortiz[3], Stephen D. Wilson[3], Ziqiang Wang[4], Rafael M. Fernandes[5] & Vidya Madhavan[1]✉

Broken time-reversal symmetry in the absence of spin order indicates the presence of unusual phases such as orbital magnetism and loop currents[1–4]. The recently discovered kagome superconductors AV_3Sb_5 (where A is K, Rb or Cs)[5,6] display an exotic charge-density-wave (CDW) state and have emerged as a strong candidate for materials hosting a loop current phase. The idea that the CDW breaks time-reversal symmetry[7–14] is, however, being intensely debated due to conflicting experimental data[15–17]. Here we use laser-coupled scanning tunnelling microscopy to study RbV_3Sb_5. By applying linearly polarized light along high-symmetry directions, we show that the relative intensities of the CDW peaks can be reversibly switched, implying a substantial electro-striction response, indicative of strong nonlinear electron–phonon coupling. A similar CDW intensity switching is observed with perpendicular magnetic fields, which implies an unusual piezo-magnetic response that, in turn, requires time-reversal symmetry breaking. We show that the simplest CDW that satisfies these constraints is an out-of-phase combination of bond charge order and loop currents that we dub a congruent CDW flux phase. Our laser scanning tunnelling microscopy data open the door to the possibility of dynamic optical control of complex quantum phenomenon in correlated materials.

Kagome lattice compounds provide an ideal platform to study novel states resulting from the interplay between topology, geometric frustration and electron correlations[18–21]. This class of materials includes magnetic metals hosting massive Dirac fermions[22–24], Weyl points[25,26] and Chern magnetism[27], as well as non-magnetic superconductors AV_3Sb_5 (where A is K, Rb or Cs)[5,6], which show correlated and topological states[28–32]. Besides superconductivity, the AV_3Sb_5 compounds host a charge-density-wave (CDW) phase that not only breaks additional rotation[15] and mirror[7] symmetries but also may break time-reversal symmetry[7–14]. The latter is particularly intriguing as broken time-reversal symmetry not driven by spins suggests orbital magnetism with staggered circulating orbital currents[7], resembling loop-current phases suggested for many decades[1–4]. In the case of AV_3Sb_5, time-reversal symmetry breaking (TRSB) has been indicated by scanning tunnelling microscopy (STM) measurements[7], muon spin-rotation experiments[8–10] and optical measurements[11,12,14]. These observations have motivated various theoretical studies of the so-called CDW flux phase, which relies on electronic correlations as the driving force behind this exotic instability[33–38]. The scenario of broken time-reversal symmetry has, however, been challenged by contradictory STM measurements[15] and by negative Sagnac interferometer measurements of spontaneous Kerr rotation[16,17].

In this work, we study the electric- and magnetic-field response of the CDW phase of the kagome superconductor RbV_3Sb_5 with a laser-coupled STM. RbV_3Sb_5 avoids the complexities associated with the coexistence of different types of bond distortion that are seen in the more commonly studied CsV_3Sb_5 compound[39–41]. The crystal structure consists of a V–Sb kagome layer sandwiched between two Sb honeycomb layers and separated by an alkaline Rb hexagonal layer[5] (Fig. 1a,b). When cleavage occurs between the Rb and Sb planes, the weakly bonded Rb adatoms can be 'swept away' with the STM tip (Supplementary Fig. 1). The clean Sb surface[42,43] (Fig. 1c,d) reveals the Sb honeycomb lattice (Supplementary Fig. 2), consistent with the crystal structure[43–45]. The Fourier transform (FT) reveals a rich pattern of charge order and Friedel oscillations (marked as $\mathbf{Q}_f$). The three Bragg peaks in the three symmetry-related Γ–M directions are labelled $\mathbf{Q}_{B1}$, $\mathbf{Q}_{B2}$ and $\mathbf{Q}_{B3}$ and the $2a_0 \times 2a_0$ CDW peaks (where a_0 is the lattice constant) along these directions are labelled $\mathbf{Q}_1$, $\mathbf{Q}_2$ and $\mathbf{Q}_3$, respectively. The unidirectional approximately $4a_0$ CDW[42–44] along the $\mathbf{Q}_2$ direction is labelled $\mathbf{Q}_{4a_0}$.

A closer look at the FT shown in Fig. 1d reveals a few interesting features. First, the intensity of the $\mathbf{Q}_2$ peak (henceforth labelled I_2) is significantly higher than the intensity of both $\mathbf{Q}_1$ (I_1) and $\mathbf{Q}_3$ (I_3). This can be seen by comparing the line profiles along three Bragg peak directions as shown in Fig. 1e, and indicates the breaking of three-fold rotational symmetry of the CDW, consistent with previous literature[7,15,43,44,46]. Theoretically, this rotation symmetry breaking has been attributed to either a staggered stacking of the CDW along the *c* axis or to an admixture of

[1]Department of Physics and Materials Research Laboratory, University of Illinois Urbana-Champaign, Urbana, IL, USA. [2]Department of Chemical Engineering and Materials Science, University of Minnesota, Minneapolis, MN, USA. [3]Materials Department, University of California Santa Barbara, Santa Barbara, CA, USA. [4]Department of Physics, Boston College, Chestnut Hill, MA, USA. [5]School of Physics and Astronomy, University of Minnesota, Minneapolis, MN, USA. [6]These authors contributed equally: Yuqing Xing, Seokjin Bae. ✉e-mail: vm1@illinois.edu

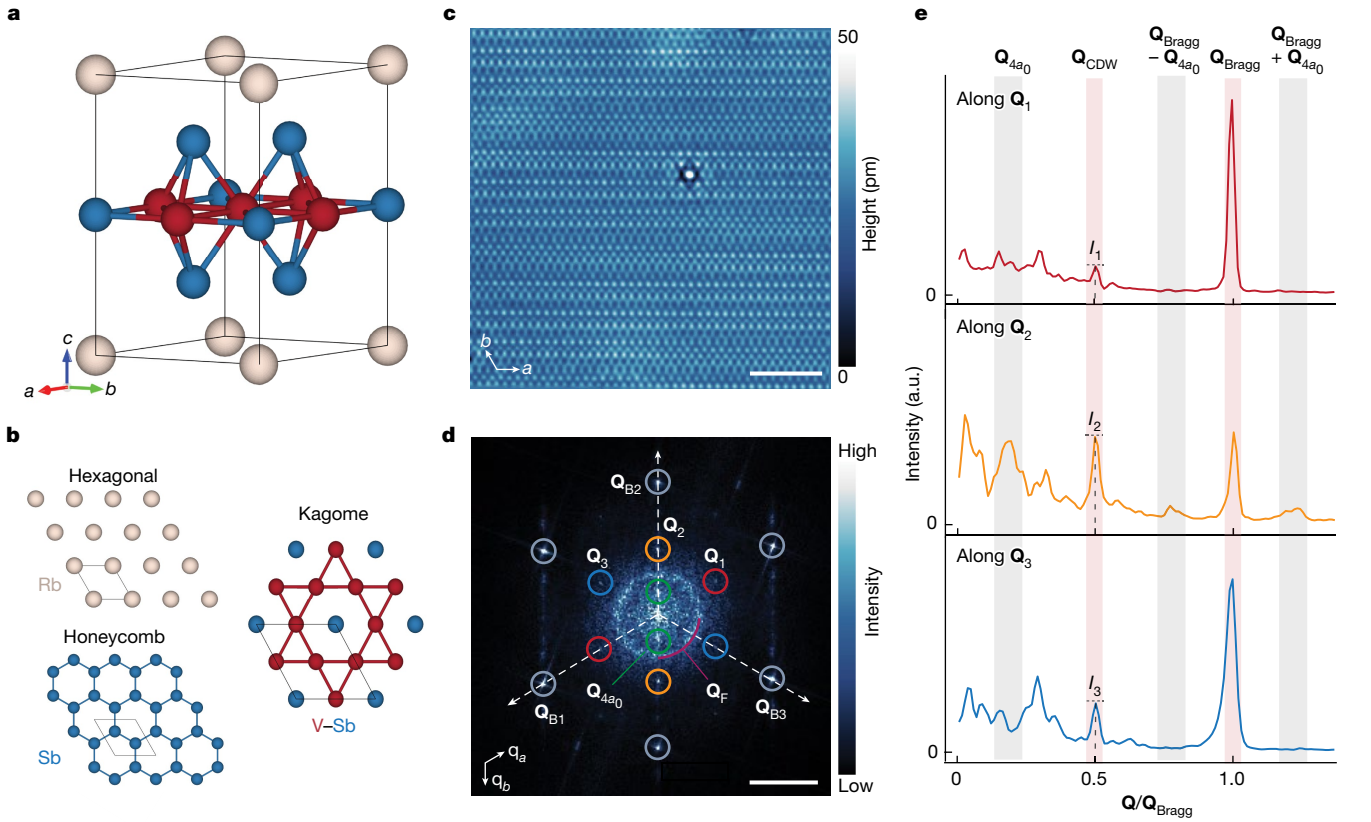

Fig. 1 | Sb surface identification of RbV_3Sb_5 and CDW peak intensities. a, Unit cell of RbV_3Sb_5. **b**, Top view of different terminations, showing the hexagonal Rb layer, the honeycomb Sb layer and the kagome V–Sb layer. **c**, Topographic image (25 nm × 25 nm) of the Sb layer (sample bias $V_s = -100$ mV, tunnelling current $I_t = 175$ pA). Scale bar, 5 nm. **d**, FT image of the Sb surface, showing the wavevectors $\mathbf{Q}_{1-3}$ associated with the $2a_0 \times 2a_0$ CDW, $\mathbf{Q}_{4a_0}$ associated with unidirectional charge order and $\mathbf{Q}_F$ associated with isotropic defect scattering related interference patterns. The three Bragg peaks along the Γ–M directions are labelled $\mathbf{Q}_{B1-B3}$. Scale bar, 0.6 Å^{-1}. **e**, Comparison of linecuts in **d** along the $\mathbf{Q}_1$ (top), $\mathbf{Q}_2$ (middle) and $\mathbf{Q}_3$ (bottom) directions. $\mathbf{Q}_{4a_0}$ and its satellite Bragg peaks are only prominent along the $\mathbf{Q}_2$ direction, while the $2a_0 \times 2a_0$ $\mathbf{Q}_{1-3}$ CDW peaks (labelled on top as $\mathbf{Q}_{CDW}$) show different intensities in the three directions.

the bond CDW with a flux phase[35,36,38,47]. Second, we find that I_1 and I_3 are also different, which indicates that vertical and diagonal mirror symmetries are also broken such that all three CDW peaks have different intensities. We will show later in the paper that the difference between I_1 and I_3 is probably due to small residual strain. The lack of mirror planes perpendicular to the kagome layer gives rise to two different senses of handedness in the CDW peak intensities, which were referred to as 'chiral' in previous STM studies[7,44], when they appeared to be switchable by applying a *c*-axis magnetic field. To understand the origin of this remarkable phenomenon, we study the response of the CDW to a different type of electromagnetic probe, that is, light.

Response of the CDW to laser illumination

A schematic of our laser-STM set-up is shown in Fig. 2a with further experimental details in Methods and Extended Data Fig. 1. Figure 2 shows the FT of the topography and the $2a_0 \times 2a_0$ CDW peak intensities before and after illumination. In this study, the laser electric field (**E**) was oriented along the in-plane Γ–M directions pointing towards either $\mathbf{Q}_1$ or $\mathbf{Q}_3$ (we henceforth label light with $\mathbf{E} \parallel \mathbf{Q}_1$ as $\mathbf{E}_1$ and $\mathbf{E} \parallel \mathbf{Q}_3$ as $\mathbf{E}_3$). $\mathbf{E}_1$ and $\mathbf{E}_3$ are along the honeycomb Sb–Sb nearest-neighbour direction in *Q* space and therefore along the V–V nearest-neighbour directions in real space. Before illumination, $I_1 > I_3$, as shown in Fig. 2c. This intensity difference is emphasized in the three-dimensional plot of just the CDW peaks (Fig. 2d). Strikingly, we find that after illumination with $\mathbf{E}_3$ (Fig. 2e,f), $I_1 < I_3$. This light-induced CDW intensity change is reversible. Illuminating the sample with $\mathbf{E}_1$ reverses the sequence of intensities again, leading to $I_1 > I_3$ (Fig. 2g,h). This finding is independent of bias voltage and can be seen in the differential conductance (d*I*/d*V*) maps (Extended Data Figs. 2 and 3). Owing to the inherent broken rotational symmetry of the CDW, I_2 always remains the strongest, so for the rest of this paper we do not discuss I_2.

To demonstrate the robustness and repeatability of the light-induced switching, we show the result of a series of laser illuminations with light polarized along either $\mathbf{E}_1$ or $\mathbf{E}_3$ in Fig. 3a. Here we plot the relative intensity $I_r = (I_1 - I_3)/\left(\frac{(I_1 + I_3)}{2}\right)$ where positive and negative I_r (marked in red or blue) correspond to a stronger I_1 or I_3, respectively (see Extended Data Fig. 4 for details on the method used to quantify the intensities). Plotting I_r rather than the absolute intensity values allows us to eliminate arbitrary intensity changes in the overall FT between measurements. Initially, before laser illumination, $I_1 > I_3$, leading to a positive I_r. After laser illumination with $\mathbf{E}_3$, I_r becomes negative ($I_1 < I_3$). As we track I_r through a sequence of light pulses, we find a one-to-one correspondence between the sign of I_r and the direction of the electric field, as shown in Fig. 3a (also see Fig. 3b for the full statistics of 33 different illuminations in an arbitrary sequence). This means that shining light along $\mathbf{E}_1$ or $\mathbf{E}_3$ always makes the intensity of the corresponding CDW peak stronger. There are three other important points to make. First, the observed laser control unequivocally proves that the intensity differences are a feature of the sample and not measurement artefacts. Second, the switching is independent of the number of pulses in an illumination and occurs even at the two-pulse limit (Fig. 3f). Finally, the laser-induced switching requires a critical fluence of about 0.2 mJ cm^{-2} (Fig. 3e).

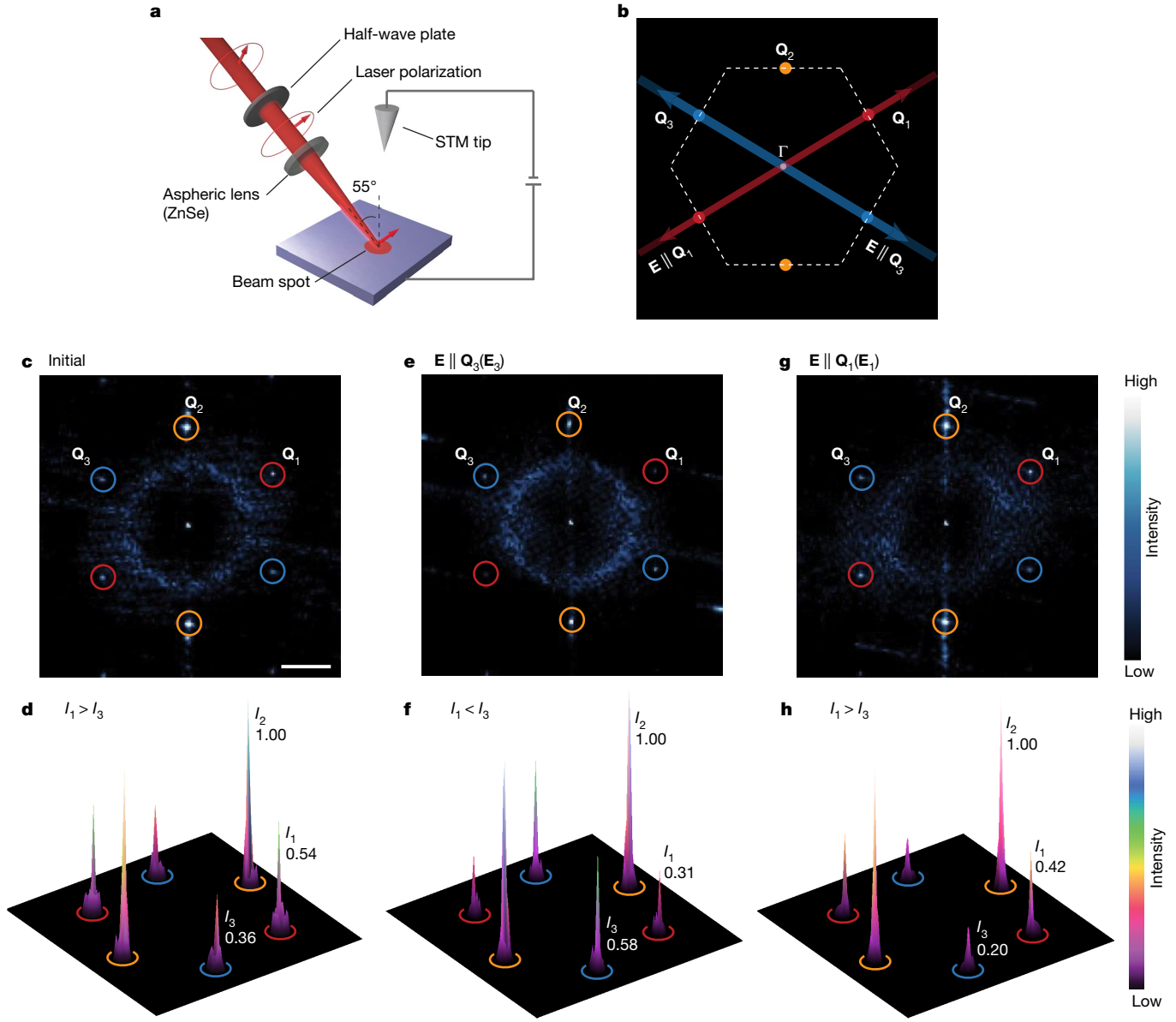

Fig. 2 | Light-induced switching of the intensity order in $2a_0 \times 2a_0$ CDW. **a**, Schematic illustration of light illumination and subsequent STM measurement on RbV_3Sb_5. A burst (2×10^5 shots at 100 kHz repetition rate) of linearly polarized, ultrafast (250 fs), near-infrared (1,025 nm) laser pulses at a fluence of 0.39 mJ cm^{-2} (unless otherwise mentioned) is used to illuminate the sample surface. **b**, Schematic FT image focusing on the $2a_0 \times 2a_0$ CDW intensity distribution. The red and blue double arrows denote the polarization direction of the laser beam. **c**, FT of topographic image before light illumination ($V_s = -100$ mV, $I_t = 175$ pA). Scale bar, 0.3 Å^{-1}. **d**, Three-dimensional view of the $2a_0 \times 2a_0$ CDW intensity peaks of **c**, showing $I_1 > I_3$. To isolate the CDW peaks, the circular quasiparticle interference pattern at the centre is masked. **e**, FT of topographic image of the same region after light illumination with linear polarization parallel to the $\mathbf{E}_3$ direction, showing that the intensities have changed upon light illumination such that $I_3 > I_1$. **f**, Three-dimensional view of **e**. **g**, FT of topographic image of the same region after light illumination with the linear polarization parallel to $\mathbf{E}_1$. **h**, Three-dimensional view of **g**, showing that the intensity order has now switched back to $I_1 > I_3$.

CDW order typically goes hand-in-hand with lattice distortions. Remarkably, we are able to directly observe such intertwining by tracking the positions of the Bragg and CDW peaks as the direction of the electric field is switched. To see this, we extract the ratio between the magnitude of the Bragg vectors that is, $\mathbf{Q}_r = |\mathbf{Q}_{B1}|/|\mathbf{Q}_{B3}|$ as an indicator of the change in the relative lattice constants after laser illumination (see Extended Data Fig. 6 for further details on how $\mathbf{Q}_B$ is determined). Figure 3c shows that $\mathbf{Q}_r$ displays the same pattern as the relative CDW intensity I_r shown in Fig. 3a. In particular, the ratio $\mathbf{Q}_r$ increases when illuminating with $\mathbf{E}_1$ and decreases when illuminating with $\mathbf{E}_3$. This means that when I_1 increases, $\mathbf{Q}_{B1}$ increases and when I_3 increases, $\mathbf{Q}_{B3}$ increases. This trend is preserved with different peak identification methods, as shown in Extended Data Fig. 7. Concomitant with the change in the Bragg momentum, the ratio between the CDW peak positions also changes (Extended Data Fig. 8) such that the $2a_0 \times 2a_0$ CDW remains commensurate after laser illumination (Fig. 3d). These combined observations suggest a strong electron–phonon coupling in this system[48] and establish that the light-induced intensity changes can be attributed to a sizable electro-striction response of the CDW state.

Response of the CDW to magnetic fields

The surprising laser-induced switching of CDW intensities observed here is similar to the previously reported magnetic-field switching of

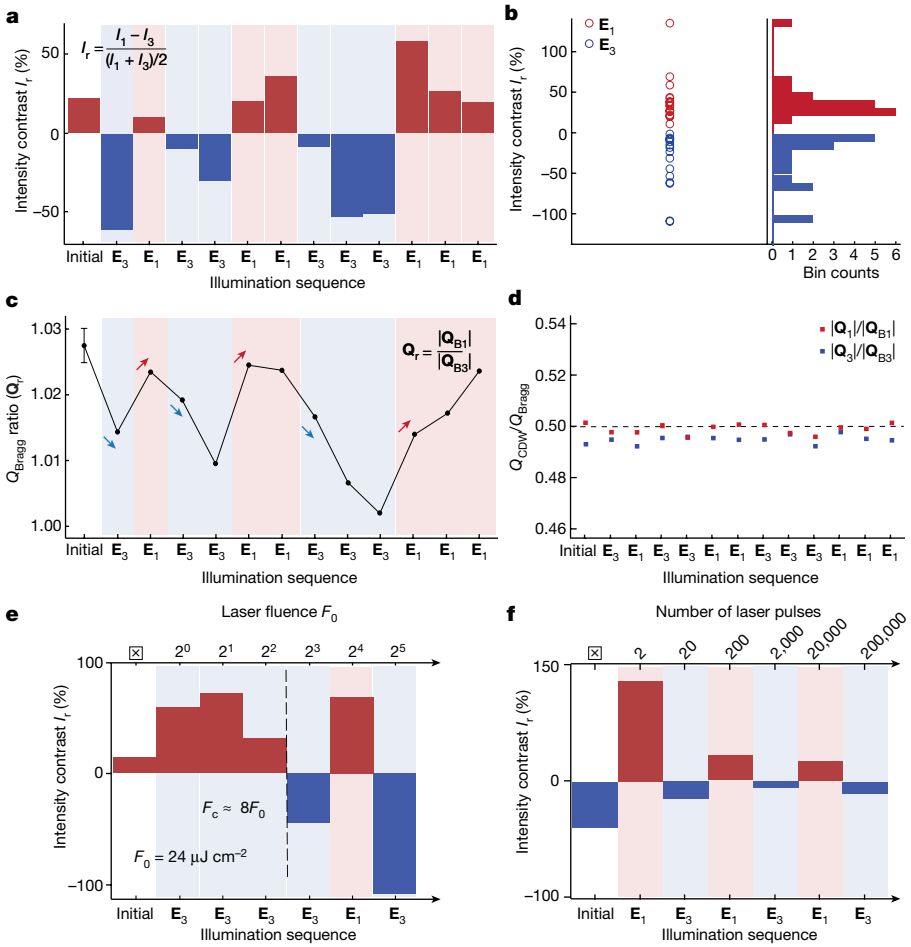

Fig. 3 | Characterization of the light-induced switching of the relative CDW intensity. a, Arbitrary illumination sequence with laser polarization along either $\mathbf{E}_1$ or $\mathbf{E}_3$. The colour of the solid bar shows the magnitude and sign of the relative intensity (I_r) as defined in the inset. The colour of the background indicates the direction of illumination. **b**, Statistics of I_r for $\mathbf{E}_1$ illuminations (red circles) and $\mathbf{E}_3$ illuminations (blue circles). On the left side, 33 bin counts in total are shown. The bin counts for a given intensity contrast range are shown on the right side. **c**, Plot of the Bragg peak ratio ($\mathbf{Q}_r$) for the arbitrary illumination sequence shown in **a**. The error bar represents the full range variation of $\mathbf{Q}_r$ in five sequential measurements of $\mathbf{Q}_r$ with circularly polarized pulsed light, which we have determined does not influence the sign of the CDW intensity contrast. **d**, Q_{CDW}/Q_{Bragg} ratio along $\mathbf{Q}_1$ (red dots) and $\mathbf{Q}_3$ directions (blue dots), showing that the $2a_0 \times 2a_0$ CDW remains commensurate during the illumination sequence. **e**, Laser pulse fluence dependence of the switching behaviour, showing that the threshold fluence to trigger the switching is about 0.2 mJ cm^{-2}. **f**, Dependence of the switching on the number of shots, showing that the CDW intensity order can be switched even with two pulses. The boxes with the crosses in **e** and **f** represent the state before laser illumination.

the relative CDW intensities[7,44]. To obtain a comprehensive picture, it is important to ascertain whether a similar magnetic-field-induced switching occurs in our samples. Figure 4a,b shows the FT of the topography under a magnetic field of −2 T. Comparing I_1 and I_3 under −2 T (Fig. 4a,b,e,f) and +2 T fields (Fig. 4c,d), we see that the relative CDW intensities switch in a reversible manner. The robustness of this magnetic-field-induced switching is illustrated by the CDW response to a sequence of out-of-plane magnetic fields (Fig. 4g). Importantly, the sign change in I_r is accompanied by a change in the relative length of the Bragg vector $\mathbf{Q}_r$ (Fig. 4h) as in the case of light-induced intensity changes. Our data thus not only provide independent confirmation of the CDW intensity reversal in magnetic fields seen previously[7,44] but also uncover that the reversal is accompanied by field-induced anisotropic strain.

Symmetry constraints on CDW order parameters

The ability to manipulate the relative intensities of the CDW peaks with linearly polarized light and magnetic field gives us valuable information on the CDW order parameter such as its relation to time-reversal symmetry. To extract this information, we employ a phenomenological analysis of the experimental results, which relies only on symmetry constraints and not on specific microscopic mechanisms. Specifically, we consider a general CDW flux phase described by a three-component CDW order parameter $\mathbf{L} = (L_1, L_2, L_3)$ with wavevectors $\mathbf{Q}_{L_1} = \left(\frac{1}{2}, 0, \frac{1}{2}\right)$, $\mathbf{Q}_{L_2} = \left(0, \frac{1}{2}, \frac{1}{2}\right)$ and $\mathbf{Q}_{L_3} = \left(-\frac{1}{2}, +\frac{1}{2}, \frac{1}{2}\right)$, corresponding to distortions of the V bonds that increase the size of the unit cell by $2 \times 2 \times 2$. We also include in the description of the flux CDW phase a TRSB CDW order parameter $\mathbf{\Phi} = (\Phi_1, \Phi_2, \Phi_3)$ with in-plane wavevectors $\mathbf{Q}_{M_1} = \left(\frac{1}{2}, 0, 0\right)$, $\mathbf{Q}_{M_2} = \left(0, \frac{1}{2}, 0\right)$ and $\mathbf{Q}_{M_3} = \left(-\frac{1}{2}, +\frac{1}{2}, 0\right)$, corresponding to V orbital magnetism ('loop currents'). Here, M_{1-3} are the in-plane projection of the CDW order parameters L_{1-3}. Our STM data gives direct access to the intensities I_1, I_2 and I_3 of the CDW peaks at $\mathbf{Q}_{M_1}$, $\mathbf{Q}_{M_2}$ and $\mathbf{Q}_{M_3}$ respectively.

In the absence of electromagnetic fields, X-ray data on RbV_3Sb_5 reveal an orthorhombic crystal structure, which is symmetric with respect to a vertical mirror[40]. As a result, two of the CDW peaks are expected to have the same magnitude—more concretely, $I_1 = I_3 \neq I_2$ if the mirror plane is chosen to include the $\mathbf{Q}_2$ wavevector. In terms of the CDW order parameters, this implies $|L_1| = |L_3| \neq |L_2|$. The fact that in our STM data I_1 and I_3 are slightly different even in the absence of electromagnetic fields is probably due to small residual strain. Our goal is to elucidate

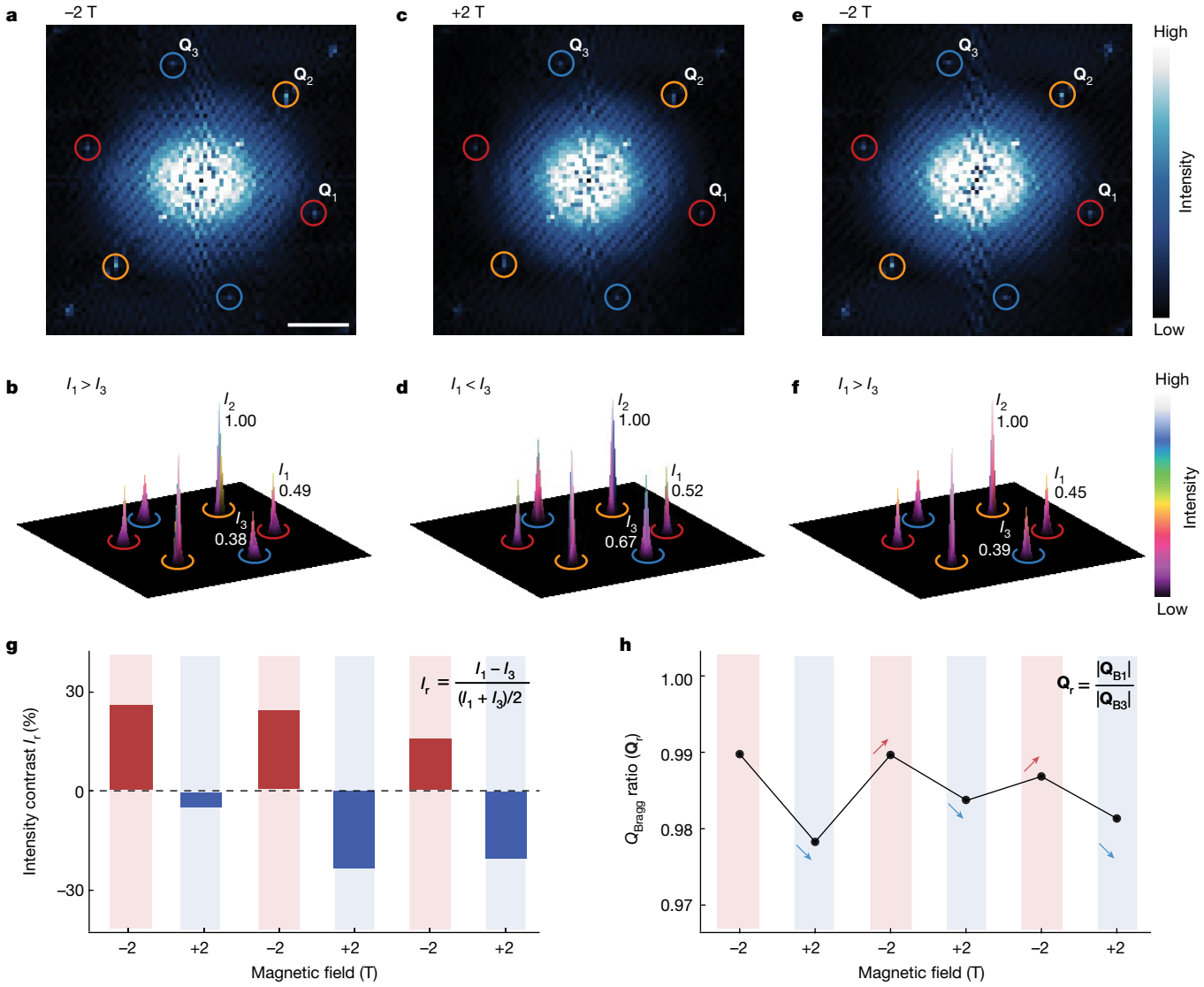

Fig. 4 | Magnetic-field-induced switching of the relative CDW intensity. **a**,**c**,**e**, FT of topography image of Sb surface at −2 T (**a**), +2 T (**c**) and −2 T (**e**) showing a switching of the relative intensities of the CDW peaks depending on the field direction. Scale bar, 0.3 Å^{-1}. **b**,**d**,**f**, Three-dimensional view of the $2a_0 \times 2a_0$ CDW peaks of **a**, **c** and **e**, respectively. The intensity of the $\mathbf{Q}_2$ CDW peak is normalized to 1.00. **g**, A plot of I_r as the magnetic-field direction is switched in a sequential fashion from negative to positive. The solid colours show the magnitude and sign of the relative intensity (I_r) as defined in the inset. The background colour indicates the direction of the magnetic field. **h**, Bragg peak ratios ($\mathbf{Q}_r$) for the magnetic-field sequence shown in **g**.

what further constraints are imposed on these CDW order parameters by the response of the CDW intensities to the electromagnetic fields.

Let us consider the light-induced response first. Incident light with polarization $\mathbf{E}_1$ or $\mathbf{E}_3$ results in a lattice distortion accompanied by $I_1 \neq I_3$ (Fig. 5a) such that the mirror plane along $\mathbf{Q}_2$ is broken. This observation suggests that the system has a non-zero electro-striction tensor element χ^{es}_{xyxy}. Such a tensor element is allowed for any CDW configuration with $|L_1| = |L_3| \neq |L_2|$, and as such does not impose additional constraints on the type of CDW order, including on the possible emergence of TRSB. It is noted that, although symmetry allows a non-zero χ^{es}_{xyxy}, it says nothing about its magnitude. The sizable effect of the 1.2-eV optical pulse on the CDW peaks, which are associated with low-energy-zone corner phonon modes, is indicative of a strong electron–phonon nonlinear coupling[48].

The response of the CDW peaks to the out-of-plane magnetic field $\mathbf{B}_z$ imposes even more severe constraints on the CDW order parameters $\mathbf{L}$ and $\mathbf{\Phi}$. The fact that the relative peak intensities I_r and the ratio of Bragg vectors $\mathbf{Q}_r$ switch with the direction of $\mathbf{B}_z$ implies a non-zero piezo-magnetic tensor element χ^{pm}_{xyz}—or, in other words, that an out-of-plane magnetic field induces an in-plane shear lattice distortion (Fig. 5b). First, this type of piezo-magnetic response necessarily implies that the CDW must break time-reversal symmetry, that is, that not only $|L_1| = |L_3| \neq |L_2|$ but also $|\Phi_1| = |\Phi_3| \neq |\Phi_2|$. Moreover, as we show in the group theoretical analysis in Methods, it implies a non-zero L_2 and a vanishing Φ_2, so that the system does not have a macroscopic magnetic dipole, and, remarkably, a non-trivial relative phase of π between the non-zero components of the two order parameters, $\mathrm{sign}(L_1 L_3 \Phi_1 \Phi_3) = -1$. This relative phase has a simple interpretation in terms of the symmetries of the bond-order pattern, described by $\mathbf{L}$, and the loop-current pattern, described by $\mathbf{\Phi}$. To illustrate this, consider the simpler case of a single kagome layer. Separately, the triple-Q bond-order pattern and the double-Q loop-current pattern each have an in-plane two-fold rotation axis (Extended Data Fig. 10a–c). The key point is that the rotation axes do not match if the aforementioned relative phase is trivial (Fig. 5c), but match when it is non-trivial (Fig. 5d). It is only in the latter case that the combined flux CDW phase has an in-plane two-fold rotation axis. This is essential for the piezo-magnetic response observed experimentally in the absence of macroscopic magnetization.

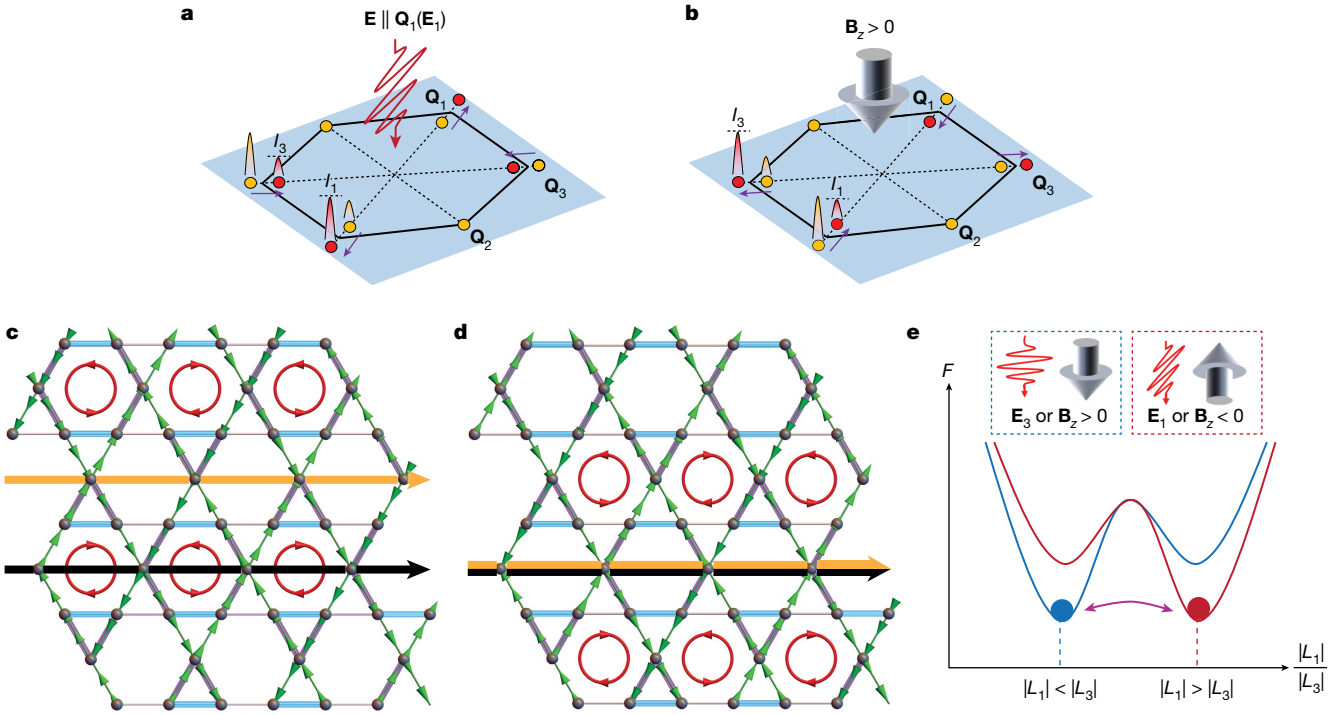

Fig. 5 | The congruent CDW flux phase. a, Schematic illustration of the electro-striction response of the system. The wavy line denotes the optical pulse. The wave amplitude direction denotes its polarization direction (here, the $\mathbf{Q}_1$ direction). The position of the red dots and purple arrows represents the response of the Bragg momentum upon illumination. **b**, Schematic illustration of the piezo-magnetic response. The grey three-dimensional arrow denotes the direction of the external magnetic field (here, positive field). **c**,**d**, An overlay view of the spatial pattern of V bond order **L** (sky-blue and purple coloured bonds) and loop-current order **Φ** (green arrows). The black and orange lines represent the in-plane two-fold rotation axes of the bond order and loop current, respectively. The red circle represents the closed current loops. **c**, For the case when the non-zero components of **Φ** and **L** have a trivial relative phase (0), **L** and **Φ** do not share the same two-fold rotation axis. **d**, For the case when the relative phase is non-trivial (π), **L** and **Φ** share the same rotation axis, resulting in a congruent CDW flux phase. **e**, Cartoon free-energy landscape of the system in terms of the components of the CDW order parameter corresponding to wavevectors $\mathbf{Q}_1$ and $\mathbf{Q}_3$ under external electromagnetic fields. It is noted that the shape of the curves is schematic and not expected to be the same for electric and magnetic fields.

Upon application of an out-of-plane magnetic field, the two-fold rotation axis is broken, resulting in a shear strain. We dub this unusual phase where the rotation axes of both the bond-order pattern and the loop-current pattern match a congruent CDW flux phase.

Discussion

A schematic of the response of the CDW, and the corresponding lattice distortions, to electric and magnetic fields is summarized in Fig. 5a,b,e. In the absence of the fields and of residual strain, the peaks at the two CDW wavevectors are equivalent ($|L_1| = |L_3|$). The application of light with polarization along a particular direction ($\mathbf{E}_1$ for instance, Fig. 5a) changes the free-energy landscape to the red curve in Fig. 5e and favours the L_1 CDW order parameter. This results in an increase in I_1 and a corresponding decrease in the lattice parameter in this direction. This finite electro-striction response is probably mediated by light-activated phonons and nonlinear electron–phonon coupling. Similarly, a magnetic field towards the sample surface (Fig. 5b) decreases the lattice parameter along the direction of the Bragg vector $\mathbf{Q}_{B3}$, resulting in an increase in the CDW intensity at $\mathbf{Q}_3$. Taken together, via its non-trivial and significant electro-striction and piezo-magnetic responses, the system can switch from one local minimum to the other within the free-energy landscape shown in Fig. 5e.

The response of the CDW to electromagnetic fields provides strong constraints on the symmetry of the order parameter. The simplest CDW configuration that satisfies these conditions is the congruent flux phase $\mathbf{L} = (|L_1|, L_2, |L_1|)$ and $\mathbf{\Phi} = (|\Phi_1|, 0, -|\Phi_1|)$, which has the magnetic space group *Cmmm* (number 65.481) and which breaks time-reversal symmetry (see group theoretical analysis in Methods). It is noted that this CDW configuration can also address several other experimental observations. First, it is consistent with one of the non-magnetic space groups (*Cmmm*, number 65) that were found to possibly refine the crystal structure of RbV_3Sb_5 through X-ray data[40]. Second, not only is it consistent with TRSB seen by muon spin-rotation experiments but also, it can reconcile the seemingly contradictory spontaneous Kerr effect results reported in the literature. Although a pristine sample would not show a spontaneous Kerr effect for this CDW configuration, as it does not have a macroscopic magnetic dipole moment, the non-zero piezo-magnetic tensor element χ^{pm}_{xyz} implies that unintentional shear strain in the sample would generate an out-of-plane magnetic moment, which in turn would give rise to a spontaneous Kerr effect. Lastly, our laser-STM study paves the way to in situ optical manipulation of strain and symmetry breaking in quantum materials.

Online content

Any methods, additional references, Nature Portfolio reporting summaries, source data, extended data, supplementary information, acknowledgements, peer review information; details of author contributions and competing interests; and statements of data and code availability are available at https://doi.org/10.1038/s41586-024-07519-5.

1. Haldane, F. D. M. Model for a quantum Hall effect without Landau levels: condensed-matter realization of the 'parity anomaly'. *Phys. Rev. Lett.* **61**, 2015–2018 (1988).
2. Hsu, T. C., Marston, J. B. & Affleck, I. Two observable features of the staggered-flux phase at nonzero doping. *Phys. Rev. B* **43**, 2866–2877 (1991).

3. Varma, C. M. Non-Fermi-liquid states and pairing instability of a general model of copper oxide metals. *Phys. Rev. B* **55**, 14554–14580 (1997).
4. Chakravarty, S., Laughlin, R. B., Morr, D. K. & Nayak, C. Hidden order in the cuprates. *Phys. Rev. B* **63**, 094503 (2001).
5. Ortiz, B. R. et al. New kagome prototype materials: discovery of KV_3Sb_5, RbV_3Sb_5, and CsV_3Sb_5. *Phys. Rev. Mater.* **3**, 094407 (2019).
6. Ortiz, B. R. et al. CsV_3Sb_5: a Z_2 topological kagome metal with a superconducting ground state. *Phys. Rev. Lett.* **125**, 247002 (2020).
7. Jiang, Y.-X. et al. Unconventional chiral charge order in kagome superconductor KV_3Sb_5. *Nat. Mater.* **20**, 1353–1357 (2021).
8. Yu, L. et al. Evidence of a hidden flux phase in the topological kagome metal CsV_3Sb_5. Preprint at https://arxiv.org/abs/2107.10714 (2021).
9. Mielke, C. et al. Time-reversal symmetry-breaking charge order in a kagome superconductor. *Nature* **602**, 245–250 (2022).
10. Khasanov, R. et al. Time-reversal symmetry broken by charge order in CsV_3Sb_5. *Phys. Rev. Res.* **4**, 023244 (2022).
11. Xu, Y. et al. Three-state nematicity and magneto-optical Kerr effect in the charge density waves in kagome superconductors. *Nat. Phys.* **18**, 1470–1475 (2022).
12. Wu, Q. et al. Simultaneous formation of two-fold rotation symmetry with charge order in the kagome superconductor CsV_3Sb_5 by optical polarization rotation measurement. *Phys. Rev. B* **106**, 205109 (2022).
13. Guo, C. et al. Switchable chiral transport in charge-ordered kagome metal CsV_3Sb_5. *Nature* **611**, 461–466 (2022).
14. Hu, Y. et al. Time-reversal symmetry breaking in charge density wave of CsV_3Sb_5 detected by polar Kerr effect. Preprint at https://arxiv.org/abs/2208.08036 (2023).
15. Li, H. et al. Rotation symmetry breaking in the normal state of a kagome superconductor KV_3Sb_5. *Nat. Phys.* **18**, 265–270 (2022).
16. Saykin, D. R. et al. High resolution polar Kerr effect studies of CsV_3Sb_5: Tests for time-reversal symmetry breaking below the charge-order transition. *Phys. Rev. Lett.* **131**, 016901 (2023).
17. Farhang, C., Wang, J., Ortiz, B. R., Wilson, S. D. & Xia, J. Unconventional specular optical rotation in the charge ordered state of Kagome metal CsV_3Sb_5. *Nat. Commun.* **14**, 5326 (2023).
18. Guo, H.-M. & Franz, M. Topological insulator on the kagome lattice. *Phys. Rev. B* **80**, 113102 (2009).
19. Tang, E., Mei, J.-W. & Wen, X.-G. High-temperature fractional quantum Hall states. *Phys. Rev. Lett.* **106**, 236802 (2011).
20. Kiesel, M. L., Platt, C. & Thomale, R. Unconventional Fermi surface instabilities in the kagome Hubbard model. *Phys. Rev. Lett.* **110**, 126405 (2013).
21. Chen, H., Niu, Q. & MacDonald, A. H. Anomalous Hall effect arising from noncollinear antiferromagnetism. *Phys. Rev. Lett.* **112**, 017205 (2014).
22. Ye, L. et al. Massive Dirac fermions in a ferromagnetic kagome metal. *Nature* **555**, 638–642 (2018).
23. Yin, J.-X. et al. Giant and anisotropic many-body spin–orbit tunability in a strongly correlated kagome magnet. *Nature* **562**, 91–95 (2018).
24. Lin, Z. et al. Flatbands and emergent ferromagnetic ordering in Fe_3Sn_2 kagome lattices. *Phys. Rev. Lett.* **121**, 096401 (2018).
25. Morali, N. et al. Fermi-arc diversity on surface terminations of the magnetic Weyl semimetal $Co_3Sn_2S_2$. *Science* **365**, 1286–1291 (2019).
26. Liu, D. F. et al. Magnetic Weyl semimetal phase in a kagomé crystal. *Science* **365**, 1282–1285 (2019).
27. Yin, J.-X. et al. Quantum-limit Chern topological magnetism in $TbMn_6Sn_6$. *Nature* **583**, 533–536 (2020).
28. Teng, X. et al. Discovery of charge density wave in a kagome lattice antiferromagnet. *Nature* **609**, 490–495 (2022).
29. Oey, Y. M. et al. Fermi level tuning and double-dome superconductivity in the kagome metal $CsV_3Sb_{5-x}Sn_x$. *Phys. Rev. Mater.* **6**, L041801 (2022).
30. Zheng, L. et al. Emergent charge order in pressurized kagome superconductor CsV_3Sb_5. *Nature* **611**, 682–687 (2022).
31. Zhong, Y. et al. Nodeless electron pairing in CsV_3Sb_5-derived kagome superconductors. *Nature* **617**, 488–492 (2023).
32. Zhu, C. C. et al. Double-dome superconductivity under pressure in the V-based kagome metals AV_3Sb_5 (A=Rb and K). *Phys. Rev. B* **105**, 094507 (2022).
33. Feng, X., Jiang, K., Wang, Z. & Hu, J. Chiral flux phase in the kagome superconductor AV_3Sb_5. *Sci. Bull.* **66**, 1384–1388 (2021).
34. Denner, M. M., Thomale, R. & Neupert, T. Analysis of charge order in the kagome metal AV_3Sb_5 (A = K, Rb, Cs). *Phys. Rev. Lett.* **127**, 217601 (2021).
35. Park, T., Ye, M. & Balents, L. Electronic instabilities of kagome metals: saddle points and Landau theory. *Phys. Rev. B* **104**, 035142 (2021).
36. Lin, Y.-P. & Nandkishore, R. M. Complex charge density waves at Van Hove singularity on hexagonal lattices: Haldane-model phase diagram and potential realization in the kagome metals AV_3Sb_5 (A = K, Rb, Cs). *Phys. Rev. B* **104**, 045122 (2021).
37. Zhou, S. & Wang, Z. Chern Fermi pocket, topological pair density wave, and charge-4e and charge-6e superconductivity in kagomé superconductors. *Nat. Commun.* **13**, 7288 (2022).
38. Christensen, M. H., Birol, T., Andersen, B. M. & Fernandes, R. M. Loop currents in AV_3Sb_5 kagome metals: multipolar and toroidal magnetic orders. *Phys. Rev. B* **106**, 144504 (2022).
39. Stahl, Q. et al. Temperature-driven reorganization of electronic order in CsV_3Sb_5. *Phys. Rev. B* **105**, 195136 (2022).
40. Kautzsch, L. et al. Structural evolution of the kagome superconductors AV_3Sb_5 (A = K, Rb, and Cs) through charge density wave order. *Phys. Rev. Mater.* **7**, 024806 (2023).
41. Xiao, Q. et al. Coexistence of multiple stacking charge density waves in kagome superconductor CsV_3Sb_5. *Phys. Rev. Res.* **5**, L012032 (2023).
42. Chen, H. et al. Roton pair density wave in a strong-coupling kagome superconductor. *Nature* **599**, 222–228 (2021).
43. Zhao, H. et al. Cascade of correlated electron states in the kagome superconductor CsV_3Sb_5. *Nature* **599**, 216–221 (2021).
44. Shumiya, N. et al. Intrinsic nature of chiral charge order in the kagome superconductor RbV_3Sb_5. *Phys. Rev. B* **104**, 035131 (2021).
45. Yu, J. et al. Evolution of electronic structure in pristine and Rb-reconstructed surfaces of kagome metal RbV_3Sb_5. *Nano Lett.* **22**, 918–925 (2022).
46. Li, H. et al. Unidirectional coherent quasiparticles in the high-temperature rotational symmetry broken phase of AV_3Sb_5 kagome superconductors. *Nat. Phys.* **19**, 637–643 (2023).
47. Christensen, M. H., Birol, T., Andersen, B. M. & Fernandes, R. M. Theory of the charge-density wave in AV_3Sb_5 kagome metals. *Phys. Rev. B* **104**, 214513 (2021).
48. Wu, P. et al. Unidirectional electron–phonon coupling in the nematic state of a kagome superconductor. *Nat. Phys.* **19**, 1143–1149 (2023).

Methods

Single-crystal growth of RbV_3Sb_5

Single crystals of RbV_3Sb_5 were synthesized from rubidium (ingot, Alfa 99.75%), vanadium (powder, Sigma 99.9%, purified in a hydrochloric acid and ethanol mixture) and antimony (shot, Alfa 99.999%) using a modified self-flux method. Inside an argon glovebox with oxygen and moisture levels <0.5 ppm, elemental reagents were weighed out to composition $Rb_{20}V_{15}Sb_{120}$, and loaded into a tungsten carbide vial to be milled for 60 min in a SPEX 8000D mill. The resulting powder was loaded into 2-ml alumina (Coorstek) crucibles and sealed inside steel tubes under argon. The sample was heated to 1,000 °C at a rate of 200 °C per hour, soaked at that temperature for 12 h, then cooled to 900 °C at a rate of 5 °C per hour, to finally be slow-cooled to 500 °C at a rate of 1 °C per hour. Single crystals of RbV_3Sb_5 were obtained and mechanically extracted, with typical dimensions of 2 mm × 2 mm × 200 μm.

Scanning tunnelling microscopy and spectroscopy

The RbV_3Sb_5 samples used in the experiments were cleaved in situ at about 90 K and immediately transferred to an STM chamber. All STM experiments were performed in an ultrahigh vacuum (1×10^{-10} mbar). Laser-coupled STM measurements were conducted under 4 K and perpendicular magnetic-field-coupled STM measurements were studied under 1.7 K. All the scanning parameters (setpoint voltage and current) of the STM topographic images are listed in the captions of the figures. Unless otherwise noted, the differential conductance (dI/dV) spectra were acquired by a standard lock-in amplifier at a modulation frequency of 913.1 Hz. The STM tip made from tungsten was fabricated by electrochemical etching.

Laser parameters, optics set-up and experimental procedure for laser-STM

The optical excitation used in this experiment was 2×10^5 burst shots of a laser pulse train at 100 kHz repetition rate and at 0.39 mJ cm^{-2} fluence (otherwise mentioned), 1,025 nm wavelength (1.21 eV) and 250 fs pulse width. The laser beam was generated by a Yb:KGW regenerative amplifier laser system (PHAROS PH2-10W, Light Conversion). The pulse-train timing was controlled by an arbitrary function generator (ARB Rider 2182, Active Technologies), which directly triggers a pulse picker inside the RA laser system. As seen from the detailed layout of the laser-STM set-up in Extended Data Fig. 1a, the beam passes through a half-wave plate for the polarization direction control. The half-wave plate rotates the polarization to a direction of interest. Then the beam is guided to the tip–sample junction area inside the USM1200LL STM (Unisoku) through a CaF_2 viewport (MPF) and ZnSe aspheric lens (Avantier), which acts as an objective lens. The focal length of the ZnSe lens at 1,025 nm was 12.43 mm. The alignment of the beam spot and the STM tip–sample junction was monitored by an optical microscope setting, which consists of another ZnSe lens, N-BK7 plano-convex lens and a complementary metal–oxide–semiconductor camera. During the alignment check, the laser beam was switched to continuous pulse-train mode and passed through a neutral density filter with optical density > 2.0 to prevent melting of the sample surface. The alignment was adjusted by moving the lens piezo stages where ZnSe lenses are mounted. The incident angle of the beam to the surface normal direction of the sample was 55°. The beam was focused to an elliptic spot (due to the incidence angle) with a size estimated to be 49 μm × 68 μm ($1/e^2$ diameter).

The procedure used for the laser-STM experiment is illustrated in Extended Data Fig. 1b. When the sample is illuminated by the laser burst shots, the tip is retracted along the surface normal by about 70 μm to prevent changes to the tip during illumination. After the burst illumination, the tip is reapproached. The lateral shift after this procedure is less than 10 nm, so it is easy to locate the cleaned Sb surface area and study the same area after every burst.

Group theoretical analysis on the response of CDW order parameter under electric and magnetic fields

Our starting point to interpret the STM data is a 'real' CDW order parameter $\mathbf{L} = (L_1, L_2, L_3)$, corresponding to in-plane and out-of-plane distortions of the V–V bonds, and an 'imaginary' CDW order parameter $\mathbf{\Phi} = (\Phi_1, \Phi_2, \Phi_3)$, which corresponds to in-plane orbital magnetic currents involving the V states. In terms of the $P6/mmm$ space group (number 191) of AV_3Sb_5, $\mathbf{L}$ transforms as the L_2^- irreducible representation (irrep). Thus, each component L_i is associated with each wavevector $\mathbf{Q}_{L_1} = \left(\frac{1}{2}, 0, \frac{1}{2}\right)$, $\mathbf{Q}_{L_2} = \left(0, \frac{1}{2}, \frac{1}{2}\right)$ and $\mathbf{Q}_{L_3} = \left(-\frac{1}{2}, +\frac{1}{2}, \frac{1}{2}\right)$, respectively; note that the three different $\mathbf{Q}_{L_i}$ are related by a three-fold rotation. In contrast, $\mathbf{\Phi}$ transforms as the mM_2^+ irrep (where m indicates that it is odd under time reversal) and thus each component Φ_i has wavevectors $\mathbf{Q}_{M_1} = \left(\frac{1}{2}, 0, 0\right)$, $\mathbf{Q}_{M_2} = \left(0, \frac{1}{2}, 0\right)$ and $\mathbf{Q}_{M_3} = \left(-\frac{1}{2}, +\frac{1}{2}, 0\right)$. Note that mM_2^+ is the simplest type of loop-current order that can be constructed out of the low-energy Van Hove singularities, corresponding to intra-orbital (or intra-Van Hove singularity) order[38]. As in density functional theory both the phonon mode L_2^- and the phonon mode M_1^+ irrep are unstable, we also consider the real CDW order parameter $\mathbf{M} = (M_1, M_2, M_3)$ for completeness[47]. Note that $\mathbf{M}$ transforms as the M_1^+ irrep and, like $\mathbf{\Phi}$, also has wavevectors $\mathbf{Q}_{M_1} = \left(\frac{1}{2}, 0, 0\right)$, $\mathbf{Q}_{M_2} = \left(0, \frac{1}{2}, 0\right)$ and $\mathbf{Q}_{M_3} = \left(-\frac{1}{2}, +\frac{1}{2}, 0\right)$. In the notation adopted here, the reciprocal lattice vectors are given by:

$$\begin{aligned} \mathbf{G}_1 &= \frac{2\pi}{a}\left(1, \frac{1}{\sqrt{3}}, 0\right) \\ \mathbf{G}_2 &= \frac{2\pi}{a}\left(0, \frac{2}{\sqrt{3}}, 0\right) \\ \mathbf{G}_3 &= \frac{2\pi}{c}(0, 0, 1) \end{aligned} \tag{1}$$

Here, a and c are the lattice parameters in real space. We start by writing down the full Landau free-energy for the coupled order parameters, $F = F_L + F_\Phi + F_M + F_{L\Phi} + F_{LM} + F_{\Phi M}$. We have, for the free terms (see also ref. 38):

$$\begin{aligned} F_L &= \frac{a_L}{2}\sum_i L_i^2 + \frac{u_L}{4}\left(\sum_i L_i^2\right)^2 + \frac{\lambda_L}{4}(L_1^2L_2^2 + L_1^2L_3^2 + L_2^2L_3^2) \\ F_\Phi &= \frac{a_\Phi}{2}\sum_i \Phi_i^2 + \frac{u_\Phi}{4}\left(\sum_i \Phi_i^2\right)^2 + \frac{\lambda_\Phi}{4}(\Phi_1^2\Phi_2^2 + \Phi_1^2\Phi_3^2 + \Phi_2^2\Phi_3^2) \\ F_M &= \frac{a_M}{2}\sum_i M_i^2 + \frac{\gamma_M}{3}M_1M_2M_3 + \frac{u_M}{4}\left(\sum_i M_i^2\right)^2 \\ &\quad + \frac{\lambda_M}{4}(M_1^2M_2^2 + M_1^2M_3^2 + M_2^2M_3^2) \end{aligned} \tag{2}$$

For the coupled terms, we obtain:

$$\begin{aligned} F_{L\Phi} &= \frac{\kappa_{L\Phi}}{4}(L_1L_2\Phi_1\Phi_2 + L_1L_3\Phi_1\Phi_3 + L_2L_3\Phi_2\Phi_3) \\ &\quad + \frac{\lambda_{L\Phi}}{4}(L_1^2\Phi_1^2 + L_2^2\Phi_2^2 + L_3^2\Phi_3^2) + \frac{u_{L\Phi}}{4}\left(\sum_i L_i^2\right)\left(\sum_i \Phi_i^2\right) \end{aligned} \tag{3}$$

as well as

$$\begin{aligned} F_{LM} &= \frac{\gamma_{LM}}{3}(L_1L_2M_3 + L_1L_3M_2 + L_2L_3M_1) \\ &\quad + \frac{\kappa_{LM}}{4}(M_1M_2L_1L_2 + M_1M_3L_1L_3 + M_2M_3L_2L_3) \\ &\quad + \frac{\lambda_{LM}}{4}(M_1^2L_1^2 + M_2^2L_2^2 + M_3^2L_3^2) + \frac{u_{LM}}{4}\left(\textstyle\sum_i M_i^2\right)\left(\textstyle\sum_i L_i^2\right) \end{aligned} \tag{4}$$

and

$$F_{\Phi M}=\frac{\gamma_{\Phi M}}{3}(\Phi_1\Phi_2M_3+\Phi_1\Phi_3M_2+\Phi_2\Phi_3M_1)+\frac{\kappa_{\Phi M}}{4}(M_1M_2\Phi_1\Phi_2+M_1M_3\Phi_1\Phi_3+M_2M_3\Phi_2\Phi_3)+\frac{\lambda_{\Phi M}}{4}(M_1^2\Phi_1^2+M_2^2\Phi_2^2+M_3^2\Phi_3^2)+\frac{u_{\Phi M}}{4}\left(\sum_i M_i^2\right)\left(\sum_i \Phi_i^2\right) \quad (5)$$

Here, the quantities a_j, u_j, γ_j, λ_j, and κ_j with subscripts $j = L$, M, and Φ are the Landau coefficients of the model whose values are material-specific. Rather than minimizing the free energy, we look for order parameter configurations that can explain the STM data. For concreteness, we will consider the instabilities driven by the **L** and **Φ** channels, such that the accompanying **M** order parameter follows trivially from the trilinear couplings γ_{LM} and $\gamma_{\Phi M}$ above.

The key quantity measured by STM is the relative intensity between the three CDW peaks at wavevectors $\mathbf{Q}_{M_1} = (1/2, 0, 0)$, $\mathbf{Q}_{M_2} = (0, 1/2, 0)$ and $\mathbf{Q}_{M_3} = (-1/2, +1/2, 0)$ which correspond to $\mathbf{Q}_1$, $\mathbf{Q}_2$ and $\mathbf{Q}_3$ in the main text. It can be conveniently described in terms of the following two-component 'vector' (see, for example, ref. 47):

$$\psi_M=\begin{pmatrix} M_1^2+M_3^2-2M_2^2 \\ \sqrt{3}\,(M_3^2-M_1^2)\end{pmatrix} \quad (6)$$

which transforms as the Γ_5^+ irrep. Indeed, if all three peaks have the same intensity, $M_1^2 = M_2^2 = M_3^2$, $\psi_M \approx (0, 0)^T$. Here, T denotes transpose. However, if one of the peaks is stronger or weaker than the other two, say $M_2^2 \neq M_1^2 = M_3^2$, then $\psi_M \approx (1\,0)^T$. The other two possibilities, corresponding to $M_1^2 \neq M_2^2 = M_3^2$ and $M_3^2 \neq M_1^2 = M_2^2$, give $\psi_M \approx (1, \sqrt{3})^T$ and $\psi_M \approx (1, -\sqrt{3})^T$. Any other non-zero value of ψ_M corresponds to three different peak intensities. Importantly, the quantity ψ_M has the same transformation properties as:

$$\psi_L=\begin{pmatrix} L_1^2+L_3^2-2L_2^2 \\ \sqrt{3}\,(L_3^2-L_1^2)\end{pmatrix} \quad (7)$$

Therefore, hereafter, we will focus only on ψ_L. The three values associated with the case where one peak is stronger or weaker than the other two equivalent peaks correspond to:

$$\psi_L^1\approx\begin{pmatrix}1\\0\end{pmatrix},\ \psi_L^2\approx\begin{pmatrix}1\\\sqrt{3}\end{pmatrix},\ \psi_L^3\approx\begin{pmatrix}1\\-\sqrt{3}\end{pmatrix} \quad (8)$$

Clearly, ψ_L^1, ψ_L^2, and ψ_L^3, are related by a 120° rotation. Therefore, if one peak becomes different to the other two, three-fold rotational symmetry is broken. It is noted, however, that there remains a vertical mirror plane—or, equivalently, an in-plane two-fold rotation axis C_2'. These results can also be obtained by noticing that the in-plane strain components $\varepsilon_{xx} - \varepsilon_{yy}$ and ε_{xy} also transform as the same Γ_5^+ irrep as ψ_M and ψ_L:

$$\varepsilon_{\parallel}=\begin{pmatrix}\varepsilon_{xx}-\varepsilon_{yy}\\-2\varepsilon_{xy}\end{pmatrix} \quad (9)$$

where $\varepsilon_{ij} \equiv (\partial_i u_j + \partial_j u_i)/2$ and **u** is the displacement vector. The coupling to the **L** order parameter is given by:

$$F_{L\varepsilon}=\alpha_1[(\varepsilon_{xx}-\varepsilon_{yy})\,(L_1^2+L_3^2-2L_2^2)-2\sqrt{3}\,\varepsilon_{xy}\,(L_3^2-L_1^2)] \quad (10)$$

where α_1 is some coupling constant. Hence, if ψ_L is in one of the three configurations described by equation (8), the system is in an orthorhombic phase, whereas for any other non-zero ψ_L values, the system is in a monoclinic phase.

We start by analysing the STM results in the absence of electromagnetic fields. Previous X-ray measurements have shown that the system is in an orthorhombic phase[40]. For concreteness, we choose the configuration corresponding to ψ_L^1, that is, $|L_1| = |L_3| \neq L_2$. From equation (10), we see that although $\varepsilon_{xx} \neq \varepsilon_{yy}$, there is no shear strain, $\varepsilon_{xy} = 0$. Moreover, in this case, the vertical mirror plane contains the reciprocal lattice vectors $\mathbf{G}_2$ and $\mathbf{G}_3$ and is thus perpendicular to the $\hat{q}_x$ axis in momentum space, $\hat{q}_x \equiv (1, -1/2, 0)$. We note that, in the experiments, the CDW peaks corresponding to L_1 and L_3 are slightly different. We attribute this behaviour to residual shear strain ε_{xy} present in the sample which, via the coupling in equation (10), induces $L_3^2 \neq L_1^2$.

Consider now the application of an in-plane electric field $E_{\parallel} = (E_x, E_y)$. As it transforms as the Γ_6^- irrep, its coupling to the L order parameter has a similar form as equation (10):

$$F_{LE}=\alpha_2[(E_x^2-E_y^2)\,(L_1^2+L_3^2-2L_2^2)-2\sqrt{3}E_xE_y\,(L_3^2-L_1^2)] \quad (11)$$

Parameterizing $E_{\parallel} = E_0(\cos\theta, \sin\theta)$ where E_0 denotes the field amplitude, we have:

$$F_{LE}=\alpha_2E_0^2[\cos2\theta\,(L_1^2+L_3^2-2L_2^2)-\sqrt{3}\sin2\theta(L_3^2-L_1^2)] \quad (12)$$

In the experiments, the electric field is applied along either the $Q_{M_1} \equiv (1/2, 0, 0) = \frac{\pi}{a}\left(1, \frac{1}{\sqrt{3}}, 0\right)$ direction or the $Q_{M_3} \equiv (-1/2, +1/2, 0) = \frac{\pi}{a}\left(-1, \frac{1}{\sqrt{3}}, 0\right)$ direction. In terms of their polar angles θ_1 and θ_3, these two directions are related according to $\theta_3 = \pi - \theta_1$. As a result, $\cos2\theta_1 = \cos2\theta_3$ but $\sin2\theta_1 = -\sin2\theta_3$. Consequently, according to equation (12), application of an electric field along these two directions leads to a splitting of the two CDW peaks, $L_3^2 - L_1^2 = \pm\delta L^2$, with opposite signs for a field along θ_1 and a field along θ_3. In terms of the strain tensor, the coupling in equation (12) can be written as:

$$F_{\varepsilon E}=\alpha_2'[(E_x^2-E_y^2)\,(\varepsilon_{xx}-\varepsilon_{yy})+4E_xE_y\varepsilon_{xy}] \quad (13)$$

From the definition of the electro-striction response tensor, $\varepsilon_{ij} = \gamma_{ijkl}E_jE_k$, we readily identify $\alpha_2' \propto \gamma_{66}$ (in Voigt notation) or, using the main text notation for γ_{ijkl}, $\alpha_2' \propto \chi^{\mathrm{es}}_{xyxy}$. This tensor element is allowed (that is, not enforced to be zero by symmetry) for both orthorhombic groups *Fmmm* and *Cmmm*, as well as for the hexagonal group *P6/mmm*. Therefore, the STM observation of a switch in the relative intensity of the CDW peaks at Q_{M_1} and Q_{M_3} when the electric-field direction is switched between the two directions does not require that the CDW breaks time-reversal symmetry.

Consider now the application of an out-of-plane magnetic field B_z, which transforms as the $m\Gamma_2^+$ irrep. The STM data show that the CDW peaks L_1^2 and L_3^2 become different, and that the relative intensity flips sign when B_z changes sign. According to equation (10), a difference in L_1^2 and L_3^2 triggers a shear distortion $\varepsilon_{xy} \neq 0$, whose sign depends on the sign of the magnetic field. Now, the piezo-magnetic response tensor is defined as $\varepsilon_{ij} = \Lambda_{ijk}B_k$. Hence, this observation implies a non-zero tensor element $\Lambda_{63} \neq 0$ (in mixed Voigt notation) or, using the notation of the main text for Λ_{ijk}, a non-zero χ^{pm}_{xyz}.

Clearly, $\Lambda_{63} \neq 0$ requires that time-reversal symmetry is broken, which suggests that the CDW phase must contain a non-zero orbital magnetic density-wave order parameter **Φ**. To identify under which configurations of **L** and **Φ** a non-zero Λ_{63} is allowed, we write down their coupling to B_z and $\varepsilon_{\parallel}$ (to leading order):

$$F_{L\Phi,B\varepsilon}=\alpha_3B_z\left[\sqrt{3}\,\varepsilon_{xy}L_2\,(\Phi_1L_3-\Phi_3L_1)+\frac{1}{2}\,(\varepsilon_{xx}-\varepsilon_{yy})\,(\Phi_1L_2L_3-2\Phi_2L_1L_3+\Phi_3L_1L_2)\right] \quad (14)$$

We can readily identify:

$$\Lambda_{63} = \alpha_3\sqrt{3}L_2(\Phi_1 L_3 - \Phi_3 L_1) \quad (15)$$

Recall that the constraints on **L** so far are $|L_1| = |L_3| \neq L_2$. A non-zero Λ_{63} further requires $|\Phi_1| = |\Phi_3|$ and $\mathrm{sign}(L_1 L_3 \Phi_1 \Phi_3) = -1$, that is it imposes constraints not only on the magnitude of the loop-current order parameter but also on the relative phase between the non-zero components of **L** and **Φ**. The second term in equation (14) also imposes the constraint $\Phi_2 = 0$, otherwise the CDW phase in the orthorhombic phase would spontaneously induce a non-zero magnetic dipole moment (as $\varepsilon_{xx} \neq \varepsilon_{yy}$), which is not observed experimentally.

The result of this analysis is that the CDW order parameter configuration consistent with the STM experimental observations is the one with $\mathbf{L} = (L_0, L_0', L_0)$ and $\mathbf{\Phi} = (\Phi_0, 0, -\Phi_0)$. From the leading-order couplings to the order parameter **M** in F_{LM} and $F_{\Phi M}$, we also find the subsidiary order $\mathbf{M} = (M_0, M_0', M_0)$, with $M_0 \approx L_0 L_0'$ and $M_0' \approx L_0^2$. We checked that this configuration results in the magnetic space group *Cmmm* (number 65.481), which indeed allows for a non-zero Λ_{63}. We extended this analysis in a systematic way to other configurations of **L** and **Φ**, as shown in the Extended Data Table 1, as well as to cases in which **Φ** transforms as other irreps, but did not find any configurations that lead to an orthorhombic magnetic space group that has $\Lambda_{63} \neq 0$.

The large number of Landau coefficients in the free energy of equations (2)–(5) makes it difficult to fully sample the ground states realized in parameter space. Nevertheless, we can identify which terms have a major role in favouring the $\mathbf{L} = (L_0, L_0', L_0)$ and $\mathbf{\Phi} = (\Phi_0, 0, -\Phi_0)$ order via a qualitative analysis. Specifically, while $\lambda_{L\Phi} < 0$ and $u_{L\Phi} < 0$ favour coexistence between **L** and **Φ** orders, the sign of $\kappa_{L\Phi}$ selects between the (L_0, L_0', L_0) and $(\Phi_0, 0, -\Phi_0)$ combination ($\kappa_{L\Phi} > 0$), which shows the desired piezo-magnetic properties, and the (L_0, L_0', L_0) and $(\Phi_0, 0, \Phi_0)$ combination ($\kappa_{L\Phi} < 0$), which does not show the desired piezo-magnetic properties. We also emphasize that the (L_0, L_0', L_0) and $(\Phi_0, 0, -\Phi_0)$ order is one of the unique ground states emerging from arbitrary combinations of **L** and **Φ**, as we verified via the ISOTROPY software. Finally, it is worth noting that, in ref. 40, where a simplified free energy for only the real CDW order parameters was studied, a rich phase diagram with various non-trivial combinations of the components of **L** and **M** was obtained.

Data availability

The data for the main figures and the Extended data figures is available at the Illinois Databank (https://doi.org/10.13012/B2IDB-4197245_V1).

Acknowledgements This material is based on work supported by the US Department of Energy Office of Science National Quantum Information Science Research Centers as part of the Q-NEXT centre, which supported the laser-STM work of S.B. and provided partial support for laser-STM development. V.M. acknowledges support from the Gordon and Betty Moore Foundation's EPiQS initiative through grant number GBMF9465 for magnetic-field STM studies and the laser-STM instrument development. Funding for sample growth was provided via the UC Santa Barbara NSF Quantum Foundry funded via the Q-AMASE-i programme under award DMR-1906325. A.N.C.S. acknowledges support from the Eddlemam Center for Quantum Innovation at UC Santa Barbara. E.R., F.Y. and T.B. were supported by NSF CAREER grant DMR-2046020. R.M.F. was supported by the Air Force Office of Scientific Research under award number FA9550-21-1-0423. Z.W. is supported by the US Department of Energy, Basic Energy Sciences (grant number DE-FG02-99ER45747) and by Research Corporation for Science Advancement (Cottrell SEED award number 27856). B.R.O. gratefully acknowledges support from the US Department of Energy (DOE), Office of Science, Basic Energy Sciences, Materials Sciences and Engineering Division.

Author contributions Y.X., S.B. and V. M. conceived the project. S.B. constructed the laser-STM set-up and designed the laser experiment. Y.X. and S.B. conducted the laser-STM measurements. Y.X. conducted the STM studies under magnetic field. A.N.C.S., B.R.O. and S.D.W. provided the RbV_3Sb_5 samples used in this study. E.R., F.Y., T.B., Z.W., and R.M.F. conducted the group theory analysis and theoretical interpretation of the data. Y.X., S.B. and V.M. performed the data analysis and wrote the paper with input from all the authors.

Competing interests The authors declare no competing interests.

Additional information
Supplementary information The online version contains supplementary material available at https://doi.org/10.1038/s41586-024-07519-5.
Correspondence and requests for materials should be addressed to Vidya Madhavan.
Peer review information *Nature* thanks Liuyan Zhao and the other, anonymous, reviewer(s) for their contribution to the peer review of this work.

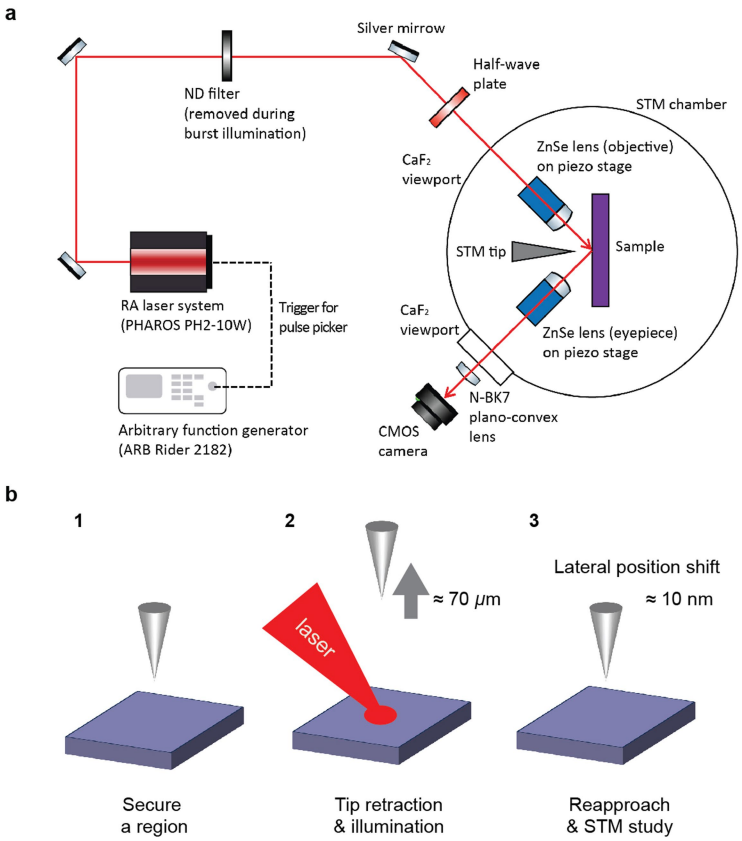

Extended Data Fig. 1 | Optics layout and experimental procedure of the laser STM. a, Optics layout of the laser STM. b, Experimental procedure to measure light-induced changes in CDW intensity.

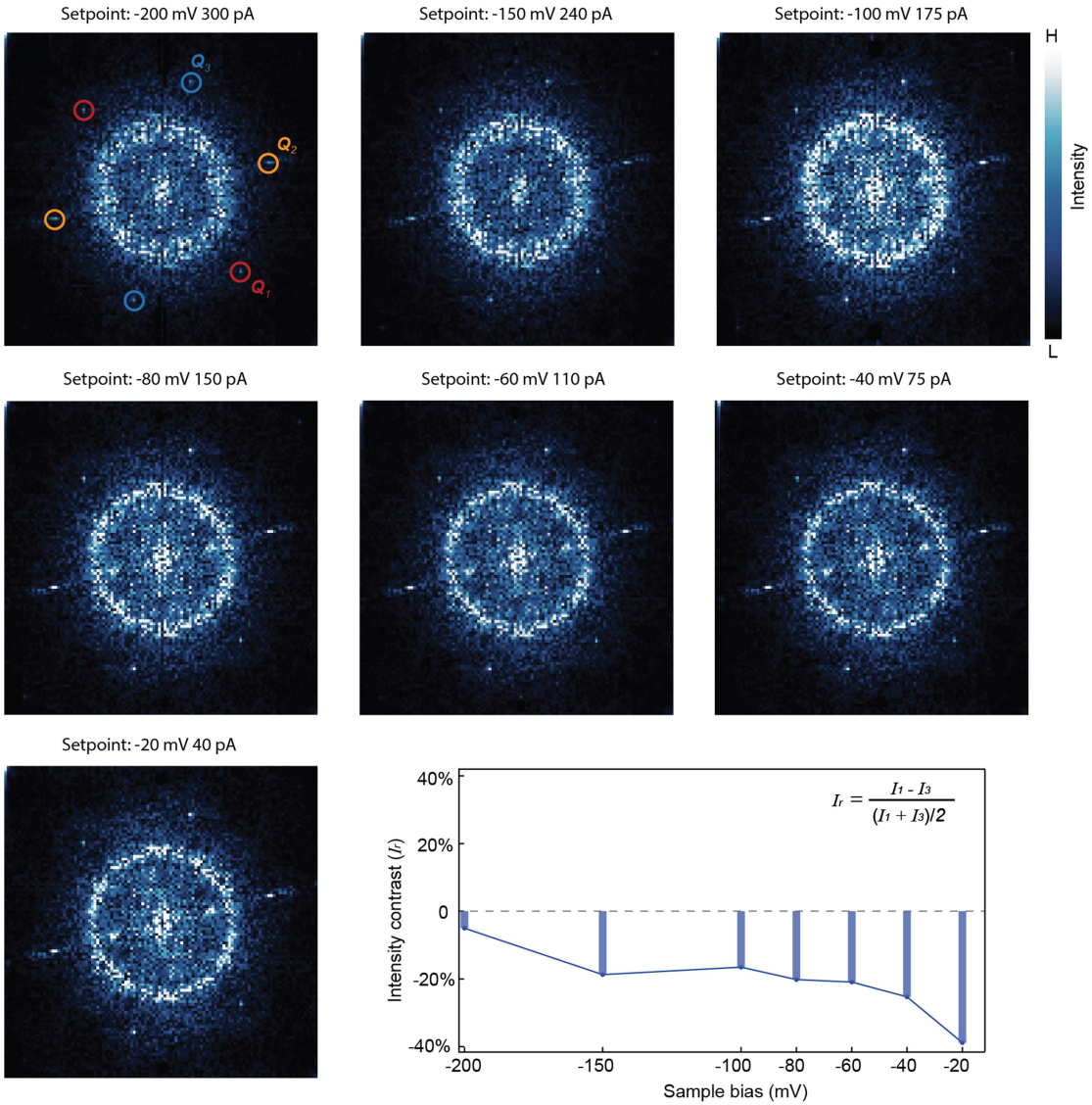

Extended Data Fig. 2 | Evolution of the CDW intensity ratio at different sample biases. For different biases, the sign of I_r remains the same.

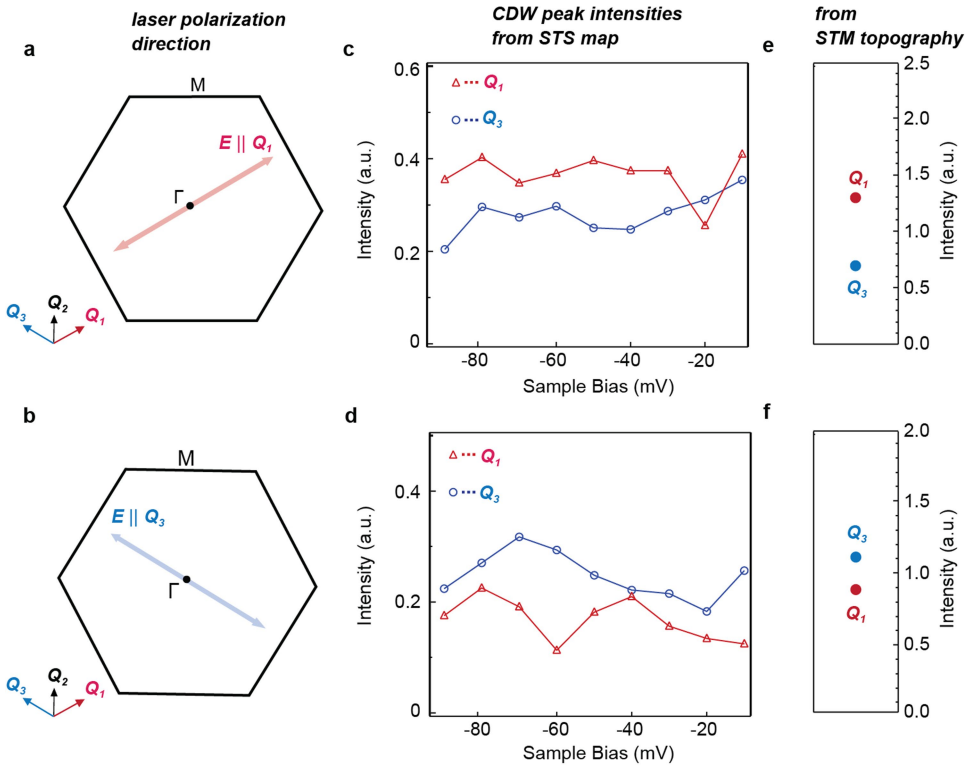

Extended Data Fig. 3 | Scanning tunneling spectroscopy (STS) maps and STM topography showing the behavior of the CDW intensity upon illumination of linearly polarized light. a-**b**, The two directions of laser polarization with respect to the schematic reciprocal lattice. The red and blue double arrows denote the polarization direction of the laser beam. Upon laser illumination along Q_1 and Q_3 directions, the same switching behaviour of the CDW intensities appears both in the STS map (**c**-**d**, V_{bias} = −200 mV, I_{set} = 100 pA) and STM topography (**e**-**f**).

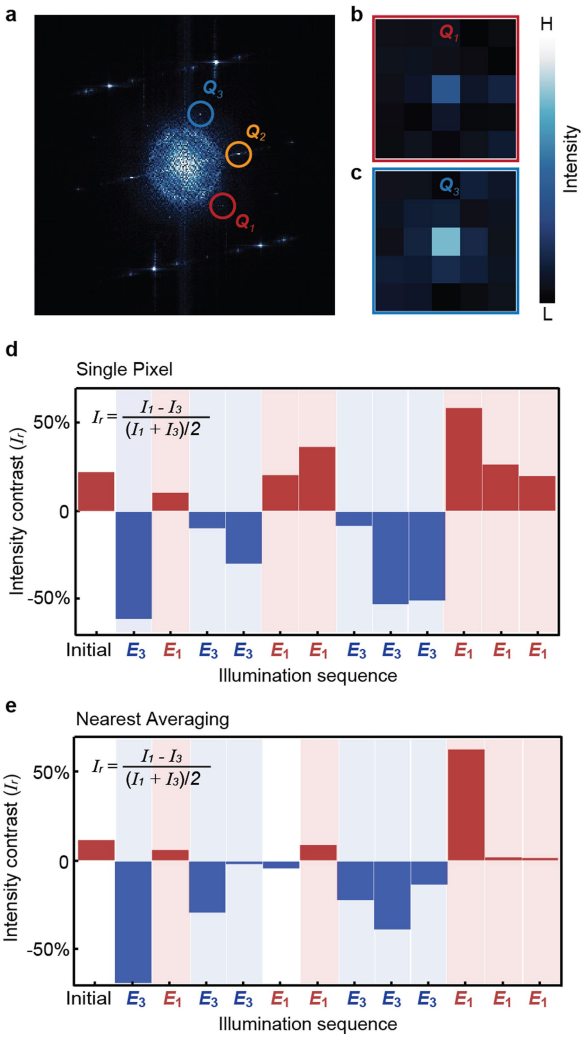

Extended Data Fig. 4 | Agreement between different methods of quantifying the CDW intensity. a, Typical FT of the Sb surface. The 2 × 2 CDW peaks along the three directions are labelled Q_1 to Q_3. **b**-**c**, Zoomed in FT images showing that the intensities of Q_1 and Q_3 are mostly localized to a single pixel. **d**, Light-induced switching of the CDW intensity with an arbitrary illumination sequence with laser polarization along either E_1 or E_3 (same as Fig. 3a), with the CDW intensities determined by the single pixel method. **e**, CDW intensity contrast along the same arbitrary illumination sequence with the nearest averaging methods (5 pixels in total). The trends in the intensity contrast remain the same while the absolute value of the intensity contrast is suppressed in most cases suggesting that using the single pixel method provides better signal.

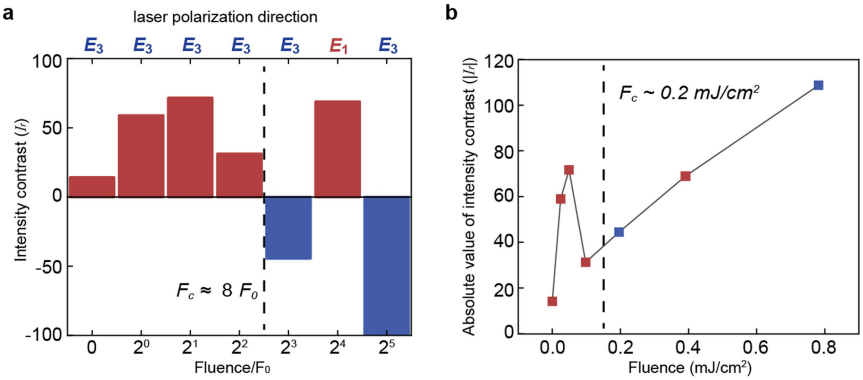

Extended Data Fig. 5 | Laser fluence dependence of the CDW intensity contrast. a, Fig. 3e in main text: $I_r = (I_1 - I_3)/2(I_1 + I_3)$ at each illumination with doubling the fluence. Beyond the critical fluence $F_c \approx 8\,F_0$, the sign of I_r starts to change depending on the direction of illumination. **b**, Absolute value of the I_r ($|I_r|$) with respect to the fluence on a linear scale. For fluence > F_c, the fluence and $|I_r|$ start to show a proportional relation.

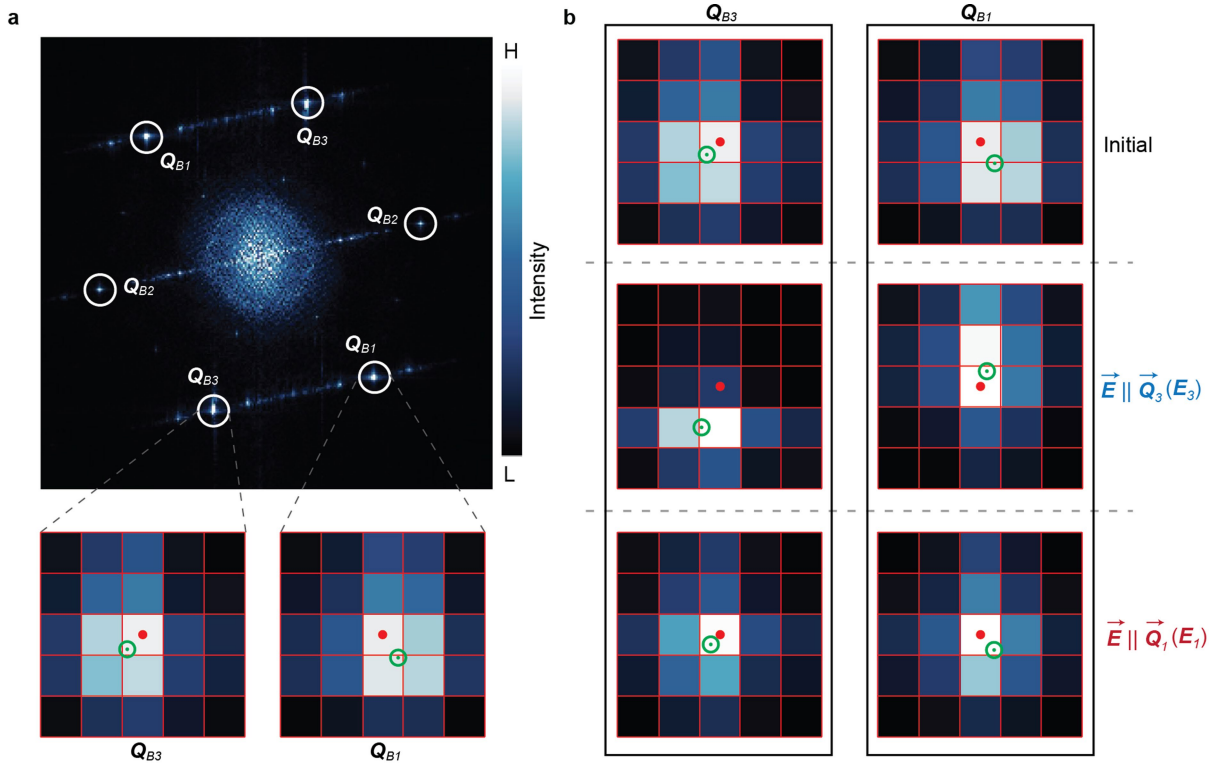

Extended Data Fig. 6 | Identification of Bragg peak vector locations. **a**, Typical FT of the Sb layer before light illumination. Bragg peaks are clearly observed and highlighted with circles. Zoom-in images of these peaks along Q_{B1} and Q_{B3} directions reveal anisotropic intensity distribution in a 5-pixel × 5-pixel size in momentum space, thus enabling us to carry out the effective center of mass to identify the actual peak location (green circles). **b**, Q_{B1} and Q_{B3} peak locations during light illumination along either E_1 or E_3 directions, showing noticeable extending/shrinking peak location. The red dot in the middle of FT serves as reference for relative peak location change.

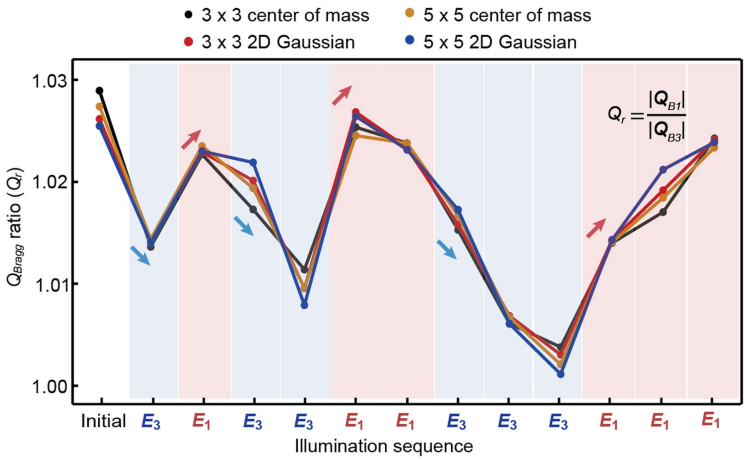

Extended Data Fig. 7 | Bragg peak ratio (Q_r) along the laser polarization sequence with different grid sizes and peak position identification methods. Different grid sizes (3 × 3 and 5 × 5) and peak position identification methods (center of mass and 2D Gaussian) show similar results for the Bragg peak ratio Q_r. This demonstrates the robustness of the trends in the Bragg peak ratio for the laser/field sequence.

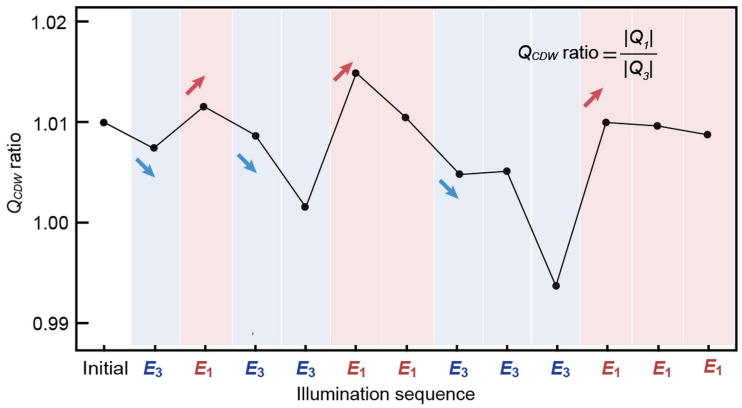

Extended Data Fig. 8 | CDW peak vector ratios of Q_1 and Q_3 for an arbitrary laser illumination sequence. During the laser illumination sequence used in Fig. 3a and c, the CDW peak ratio shows the same pattern trend as the relative CDW intensity I_r (Fig. 3a) and Q_{Bragg} ratio Q_r (Fig. 3c).

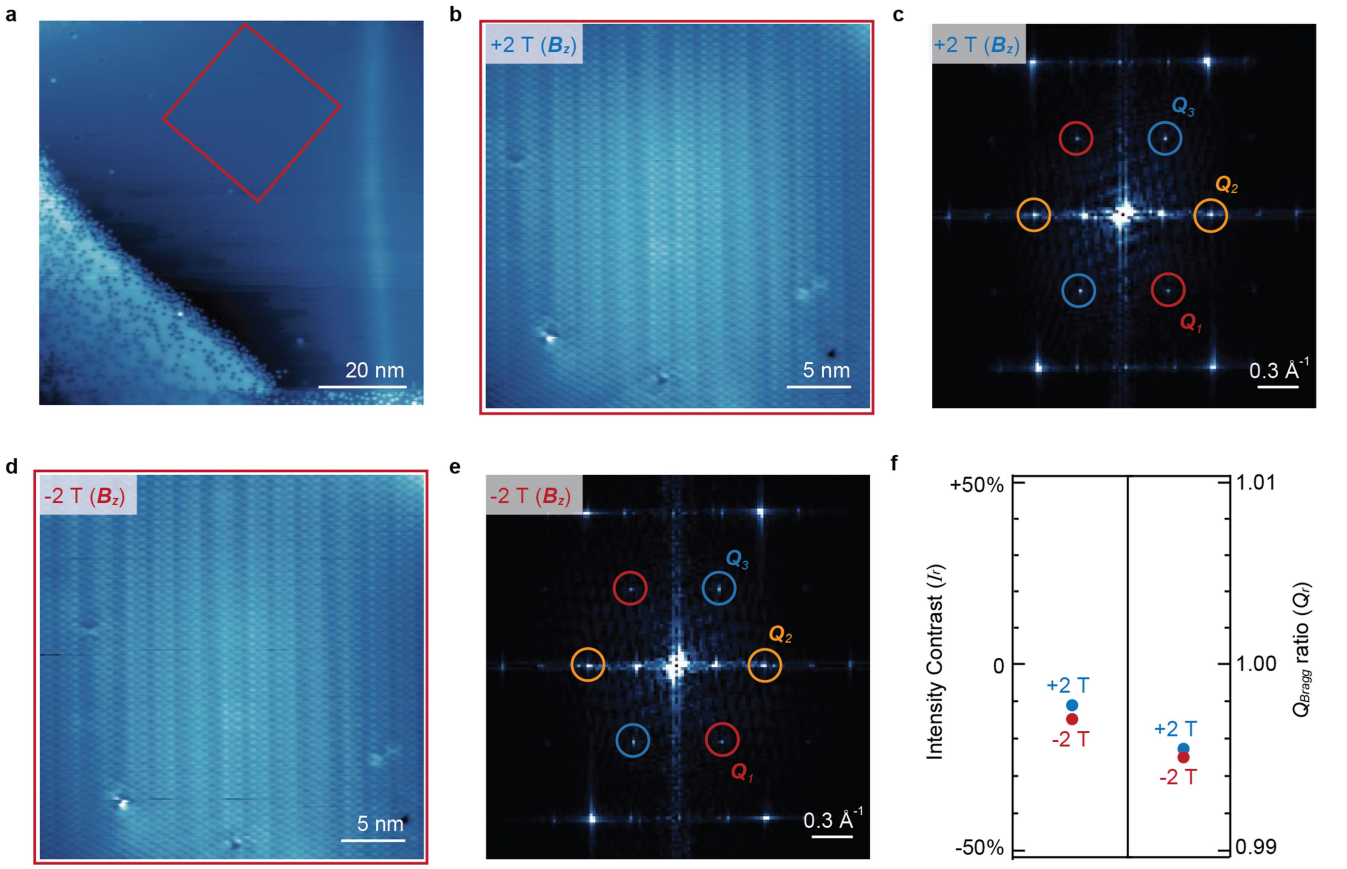

Extended Data Fig. 9 | Data on a strained region where the CDW intensity contrast and Bragg vector ratio do not respond to the magnetic field. **a**, Large scale topography image (~87 nm × 87 nm) of the post-cleaned region. A wrinkle is clearly observed, indicating the presence of the strong residual in-plane strain in this region. **b**,**d**, Zoom-in topography image (30 nm × 30 nm) of the same region under +2 T and −2 T magnetic field perpendicular to the sample surface. **c**,**e**, FTs of (b) and (d) show a robust intensity order between Q_1 and Q_3 with respect to the opposite directions of out-of-plane magnetic field. **f**, Intensity contrast plot (Q_r in left panel) and Bragg vector ratio (Q_r in right panel) from this region. The intensity contrast does not show a sign change between + 2 and −2 T field. The Bragg vector ratio shows a marginal change (≈0.0005) compared to the case (≈0.01, Fig. 4h) where there is a flip in the sign of the CDW intensity contrast (Fig. 4g).

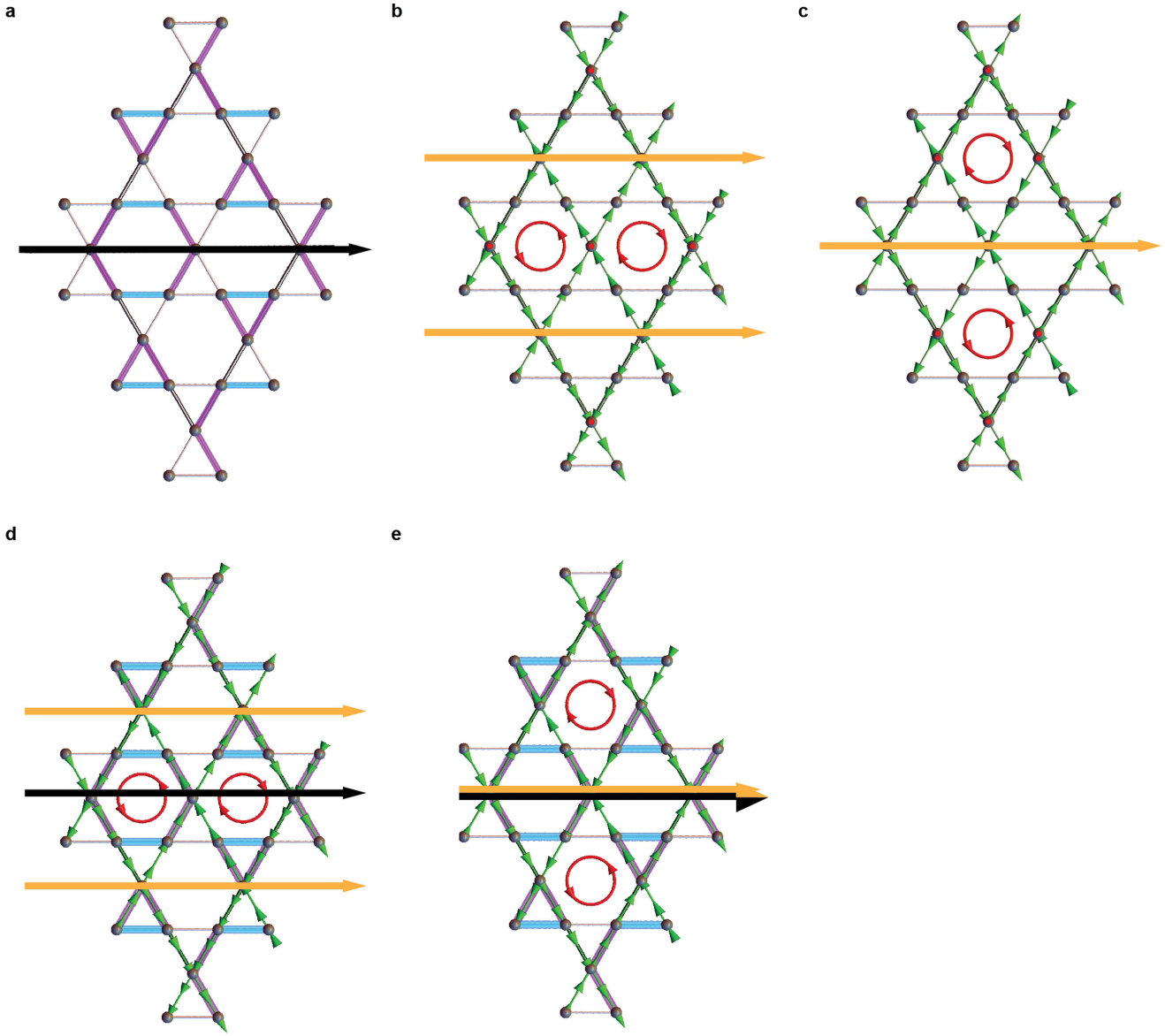

Extended Data Fig. 10 | Vanadium bond order and loop current pattern and their rotation axis for different order parameter configurations. **a**, Vanadium bond-order pattern (colored bonds) for the 3Q "real" CDW order parameter configuration $\mathbf{L} = (L, L', L)$ on a single kagome layer. The black line denotes the in-plane 2-fold rotation axis. **b**, Loop-current pattern (green arrows) for the 2Q "imaginary" CDW order parameter configuration $\mathbf{\Phi} = (\Phi, 0, \Phi)$, whose relative phase between its non-zero components is trivial. The 2-fold rotation axis is denoted as the orange lines. The closed current loops are denoted as red circles. **c**, Loop-current pattern for the 2Q "imaginary" CDW order parameter configuration $\mathbf{\Phi} = (\Phi, 0, -\Phi)$. There exists a relative π phase between the non-zero components, which changes the location of the 2-fold rotation axis. **d**, An overlay view of the $L_1 = L_3 \neq L_2$ and $\Phi_1 = \Phi_3$ orderings. In this case, bond-order and loop-current patterns have different rotation axis so that the 2-fold rotation is broken in the system, which allows a macroscopic out-of-plane magnetic dipole moment. **e**, An overlay view of the $L_1 = L_3 \neq L_2$ and $\Phi_1 = -\Phi_3$ orderings. In this case, both bond-order and loop-current patterns share the same rotation axis, so that the system possesses an in-plane 2-fold rotation axis, which forbids a macroscopic magnetic dipole moment. This configuration allows the system to have piezo-magnetic effect even in the absence of a macroscopic magnetic dipole moment.

Extended Data Table 1 | Magnetic space groups for different combinations of the bond-order CDW and the loop-current CDW order parameters

L_2^- bond-order CDW	mM_2^+ loop-current CDW	Magnetic Space Group	Macroscopic Magnetization	Nonzero Components of Piezomagnetic Tensor
$L_1 = L_2 \neq L_3$	$\Phi_1 = -\Phi_2, \Phi_3 = 0$	*Cmmm* (#65.481)	none	$yzx = zyx$ $xzy = zxy$ $xyz = yxz$
$L_1 = -L_2, L_3 = 0$	$\Phi_1 = \Phi_2, \Phi_3 = 0$	$C_A mmm$ (#65.490)	none	none
$L_1 = -L_2, L_3 = 0$	$\Phi_1 = -\Phi_2, \Phi_3 = 0$	$C_A ccm$ (#66.500)	none	none
$L_1 = L_2 \neq L_3$	$\Phi_1 = \Phi_2 \neq \Phi_3$ (Φ_3 may be zero)	*Cm'm'm* (#65.485)	M_z	xxz yyz zzz $yzy = zyy$ $xzx = zxx$
$L_1 \neq L_2 \neq L_3$	$\Phi_1 \neq \Phi_2 \neq \Phi_3$	*P2/m* (#10.42)	M_z	yyz zzz xxz zxy zxx yxz yzy yzx

Of the possibilities considered, only the congruent CDW phase exhibits the required piezo-magnetism in the absence of macroscopic magnetization. Note that the combination of order parameter $L_1 = L_2 \neq L_3$ and $\Phi_1 = -\Phi_2 \neq \Phi_3$ with $\Phi_3 \neq 0$ reduces the symmetry down to monoclinic *P2/m*, where none of the order parameters components remain equal.